INAR
INSTITUTE FOR ATMOSPHERIC AND EARTH SYSTEM RESEARCH

Master's thesis
Meteorology

The impact of thermal turbulence on flow conditions in a real street canyon using large-eddy simulations

Jani Juhani Strömberg

18.08.2021

Supervisor(s): Assoc. Prof. Leena Järvi
PhD Mona Kurppa

Censor(s): Assoc. Prof. Leena Järvi
PhD Mona Kurppa

UNIVERSITY OF HELSINKI
Master's Programme in Atmospheric Sciences

Gustaf Hällströmin katu 2, 00560 Helsinki
FI-00014 University of Helsinki

HELSINGIN YLIOPISTO — HELSINGFORS UNIVERSITET — UNIVERSITY OF HELSINKI

Tiedekunta — Fakultet — Faculty	Koulutusohjelma — Utbildningsprogram — Education programme
Faculty of Science	Master's Programme in Atmospheric Sciences

Tekijä — Författare — Author
Jani Juhani Strömberg

Työn nimi — Arbetets titel — Title

The impact of thermal turbulence on flow conditions in a real street canyon using large-eddy simulations

Opintosuunta — Studieinriktning — Study track
Meteorology

Työn laji — Arbetets art — Level	Aika — Datum — Month and year	Sivumäärä — Sidoantal — Number of pages
Master's thesis	18.08.2021	46 pages

Tiivistelmä — Referat — Abstract

Air temperatures are commonly higher in urban environments compared to rural ones. The energy input of solar radiation and its storage in urban surfaces changes the way the surface interacts with the atmosphere through turbulent fluxes and mixing processes. The complexity of radiative properties combined with the effect of urban geometry makes the magnitude of the effect radiation has on the dynamics of boundary layer flow an important area of study. The aim of this study is to understand and quantify how much the radiative processes alter the flow field and turbulence in a real urban street canyon in Helsinki.

The model used is the large-eddy simulation (LES) model PALM, which solves for the flow and the most relevant atmospheric scales that describe interactions between the surface and atmosphere. An additional library called RRTMG (Rapid Radiative Transfer Model for Global Models) is used in this study to provide the radiation input impacting the boundary layer flow. Two embedded surface models in PALM, USM (Urban Surface Model) and LSM (Land-Surface Model) are used to solve the local conditions for radiative balance based on the output of RRTMG. Two model runs are made (RRTMG On & RRTMG Off), both identical in terms of the large-scale forcing boundary conditions and land-use data, but with additional radiation input in RRTMG On.

The results show that radiation alters the low level stratification of potential temperature, which leads to more unstable conditions. Near-surface air temperatures within the canyon were increased by 3.9°C on average. Horizontal wind speeds increased by 76% close to the ground compared to RRTMG Off. RRTMG On also showed a change in the structure of the topographically forced canyon vortex, as the low wind conditions enabled the radiative effects to have a stronger effect in its forcing. The center of the vortex changed in location more towards the center of the canyon and the vertical motions on opposing sides of the street were strengthened by 0.15 $\frac{\mathrm{m}}{\mathrm{s}}$ in both vertical directions. Additionally both mechanical and thermal turbulence production increased with RRTMG On, while the thermal production remained smaller by one magnitude compared to mechanical production within Mäkelänkatu. Higher wind speeds and their variance gave rise to increased mechanical production of turbulence and radiative effects increased the thermal production. More research is however needed to determine thermal turbulence's role in situations with different meteorological conditions or in other cities.

Avainsanat — Nyckelord — Keywords
Meteorology, Turbulence, LES, Urban meteorology, Radiation, CFD, TKE

Säilytyspaikka — Förvaringsställe — Where deposited

Muita tietoja — övriga uppgifter — Additional information

HELSINGIN YLIOPISTO — HELSINGFORS UNIVERSITET — UNIVERSITY OF HELSINKI

Tiedekunta — Fakultet — Faculty	Koulutusohjelma — Utbildningsprogram — Education programme
Matemaattis-luonnontieteellinen tiedekunta	Ilmakehätieteiden maisteriohjelma

Tekijä — Författare — Author
Jani Juhani Strömberg

Työn nimi — Arbetets titel — Title

The impact of thermal turbulence on flow conditions in a real street canyon using large-eddy simulations

Opintosuunta — Studieinriktning — Study track
Meteorologia

Työn laji — Arbetets art — Level	Aika — Datum — Month and year	Sivumäärä — Sidoantal — Number of pages
Pro gradu	18.08.2021	46 sivua

Tiivistelmä — Referat — Abstract

Ilman lämpötilat ovat yleisesti korkeampia rakennetuilla alueilla verrattuna ympäristöön. Auringon säteily ja sen varastoituminen rakennetuille pinnoille muuttavat pinnan vuorovaikutusta ilmakehän kanssa voiden ja sekoitusprosessien kautta. Säteilyprosessien monimutkaisuus yhdistettynä rakennettuun geometriaan tekee näistä prosesseista tärkeän tutkimuskohteen, jotta voitaisiin määrittää, kuinka suuri vaikutus säteilyllä on rajakerroksen dynamiikkaan. Tämän tutkimuksen tavoite on ymmärtää ja määrittää miten säteilyprosessit muuttavat virtauskenttää ja turbulenssia Helsingin Mäkelänkadun katukuilussa.

Tässä tutkimuksessa käytetään LES-mallia PALM, joka ratkaisee virtauksen ja keskeisimmät virtausrakenteet ilmakehän ja pinnan vuorovaikutuksessa. Erillistä säteilymallia nimeltä RRTMG käytetään tuottamaan muuttujat, jotka vaikuttavat rajakerroksen prosesseihin. Kahta PALMiin sulautettua pintamallia, USM ja LSM, käytetään ratkaisemaan paikallinen säteilytase RRTMG:n tuottaman informaation perusteella. Tässä tutkimuksessa ajetaan kaksi malliajoa (RRTMG On & RRTMG Off), jotka ovat ilmakehän suuren skaalan pakotteiden ja maankäytön perusteella identtisiä, mutta säteilymallin tuottama informaatio lisättynä ajoon RRTMG On.

Tulokset osoittavat, että säteily muuttaa alempien kerrosten kerrostuneisuutta, mikä johtaa epästabiiliin tilanteeseen. Ilman lämpötilat katukuilussa nousivat 3.9°C. Vaakasuuntaiset tuulet voimistuivat 76% maanpinnan lähellä verrattuna ajoon RRTMG Off. RRTMG On:ssa topografian pakottamana syntynyt katupyörre muuttui myös rakenteeltaan, kun vähätuulisen tilanteen johdosta säteilyprosesseilla on suurempi vaikutus pyörteen muodostumisessa. Pyörteen keskuksen sijainti siirtyi kohti katukuilun keskustaa ja vastakkaisilla puolella erisuuntaisten tuulten voimakkuudet voimistuivat 0.15 $\frac{\mathrm{m}}{\mathrm{s}}$. Lisäksi mekaanisen ja termisen turbulenssin tuotto kasvoi ajossa RRTMG On, mutta terminen tuotto on kertaluokkaa pienempää, kuin mekaaninen tuotto katukuilun alueella. Suuremmat tuulen nopeudet ja niiden vaihtelu voimistivat mekaanista turbulenssin tuottoa, kun taas säteilyprosessien ratkaisu nosti termistä tuottoa epästabiilissa tapauksessa. Lisää tutkimusta tarvitaan määrittämään termisen turbulenssin rooli eri meteorologisissa tilanteissa tai muissa kaupungissa.

Avainsanat — Nyckelord — Keywords
Meteorologia, Turbulenssi, LES, Urbaani meteorologia, Säteily, CFD, TKE

Säilytyspaikka — Förvaringsställe — Where deposited

Muita tietoja — övriga uppgifter — Additional information

Contents

1. Introduction

The increased occurrence of heatwaves globally due to climate change has been suggested across multiple studies (Meehl and Tebaldi, 2004; Guerreiro et al., 2018). This phenomenon as a research topic is becoming more important as up to 55% (2018) of the global population live in urban areas, which is projected to reach 68% by 2050 (United Nations, 2019). This has lead to city planners focusing more on mitigation strategies to improve thermal comfort, but still ensure that street ventilation and air quality are not compromised (Gross, 2012; Karttunen, 2020; Santamouris and Yun, 2020). Ventilation depends on radiative processes as there is more production of turbulence when solar radiation is present, which leads to increased mixing of air (Park et al., 2017). Therefore, understanding the effect thermal turbulence production can have on urban air is important to accurately describe thermal comfort and ventilation.

Urban areas are characterized by increased turbulence due to rough surfaces, such as sharp edges of buildings, and higher temperatures due to lack of vegetative areas, which would normally act as a buffer that mitigate large changes in surface temperatures (Stull, 1988; Oke, 1987). The amount of disturbance to flow depends on the type of building layout and the shape of the buildings themselves. Urban areas have a higher building density compared to rural areas, which disturbs the mean flow more and limits the ventilation of air (Santamouris and Yun, 2020; Park and Baik, 2013). Higher building layout density decreases ventilation and increases reflections within street canyons, essentially trapping longwave and shortwave radiation by decreasing the sky-view factor (SVF) (Oke, 1987; Park et al., 2017). The overall decrease in vegetation and high thermal capacity of human made surfaces lead to a phenomenon called the urban heat island

(UHI), which is characterized by temperatures that are several degrees higher compared to surrounding rural environments in large cities (Oke, 1988; Santamouris and Yun, 2020). The effect of thermal turbulence can have a positive impact on thermal comfort in cities due to the increased mixing with the overlying air (Oke, 1987).

Turbulence and street canyon flow in general have been researched intensively in recent years through modeling (Kurppa et al., 2020b; Park and Baik, 2013). LES (Large-Eddy Simulation) modeling provides a way to solve the three-dimensional wind components and other variables describing boundary layer flows with high spatial and temporal resolutions (Maronga et al., 2020; Belda et al., 2020). Most of these simulations have not yet included the effect of solar radiation induced thermal turbulence on street canyon flow patterns and temperature distributions (Kurppa et al., 2020b; Karttunen, 2020). Earlier simulations have rather focused on simplified radiation schemes or heating parameterization through other means (Park and Baik, 2013; Nazarian et al., 2020). Implementing a radiation scheme to an LES model offers a way to model the complex radiative transfer processes in urban areas, such as multiple reflections, diffuse radiation and the effect of shading and the resulting thermal effects on flow structures (Salim et al., 2020). Individual physical properties of surfaces such as their porosity, thermal capacity and emissivity all have an effect on how high the surface temperatures can reach and also how much heat is released during the night (Krč et al., 2021; Mirzanamadi et al., 2018).

This thesis aims to describe how the inclusion of radiative processes alters the flow and turbulence in a real street canyon in Helsinki. The LES model, PALM, is used and coupled with the radiation module RRTMG (Rapid Radiative Transger Model for Global models). Large-scale forcing is supplied from the numerical weather prediction model MEPS/HARMONIE. The analysis methods used include studying the difference in flow patterns and temperatures in a neighborhood scale and in a local street canyon scale. Profiles, cross sections and their temporal and spatial averages are used in estimating the impact of radiation at different heights. The central focus is in the Mäkelänkatu

street canyon and its environment, with an additional look into the overall situation in surrounding areas.

2. Theory

This chapter introduces the underlying theory relevant for this thesis. It relies mostly on Stull (1988); Oke (1988, 1987), with additional insight into other sources.

2.1 Planetary boundary layer

2.1.1 Characteristics

The planetary boundary layer (PBL) describes the air layer closest to Earth's surface, which has a thickness ranging from 0.1 to 3 kilometers and responds to surface forcings within a timescale of one hour (Stull, 1988). The mean flow of air in the free atmosphere does not have any opposing objects that would redirect or slow down the flow. In the boundary layer, however, the close vicinity of surface elements such as buildings, trees and hills all the way to large mountain ranges directly interfere with the mean flow, with the strongest resistive forces closer to the ground. These objects disturb the mean flow and induce fluctuations which result in turbulence. The turbulent nature of the PBL is the main feature that separates it from the free atmosphere (Stull, 1988; Oke, 1988). Figure **??** shows the generalized structure of the troposphere, with a deep free atmosphere and a thinner boundary layer near the surface. Depending on the time of day and the altitude from the ground, the UBL can be divided into its own separate components (Stull, 1988). These components include the mixed layer (ML), residual layer (RL) and the stable boundary layer (SBL). Closest to the ground is where the surface layer (SL) is located, which is characterized by turbulent variations in fluxes and stress being less than

10% of their magnitude. Monin-obukhov similarity theory (MOST) is a type of scaling similarity typically used in the SL. It describes the vertical profiles of nondimensionalized mean flow and turbulence with Monin-Obukhov parameters. As the sun sets and the solar heating stops, a residual layer forms with a neutral stratification on top of a stable layer closer to ground. These layers are visually represented in Figure 2.2, with the mixing layer residing over the surface layer, both of which are contained within the PBL.

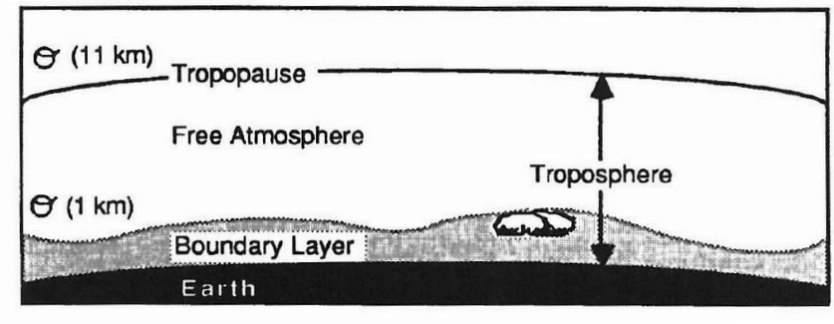

Figure 2.1: Structure of the lowest layers of the atmosphere on earth (Stull, 1988).

2.1.2 Urban boundary layer

Urban areas built with solid surfaces such as concrete and brick buildings and pavements cause the urban boundary layer (UBL) to have different characteristics than for example the boundary layer over a lake or a forest (Stull, 1988; Oke, 1988). The different human-made surface materials have typically large heat capacities and low albedos, which means they store more heat and can reach high temperatures on clear summer days (Mirzanamadi et al., 2018; Dylla, 2019). These temperatures can be quite extreme, with for example asphalt reaching up to 70°C on clear summer days. The lack of moisture from vegetation and with cars and heating as great sources of anthropogenic heat, urban areas are often a few degrees warmer than their surroundings, and this is called the urban heat island effect (UHI) (Oke, 1988).

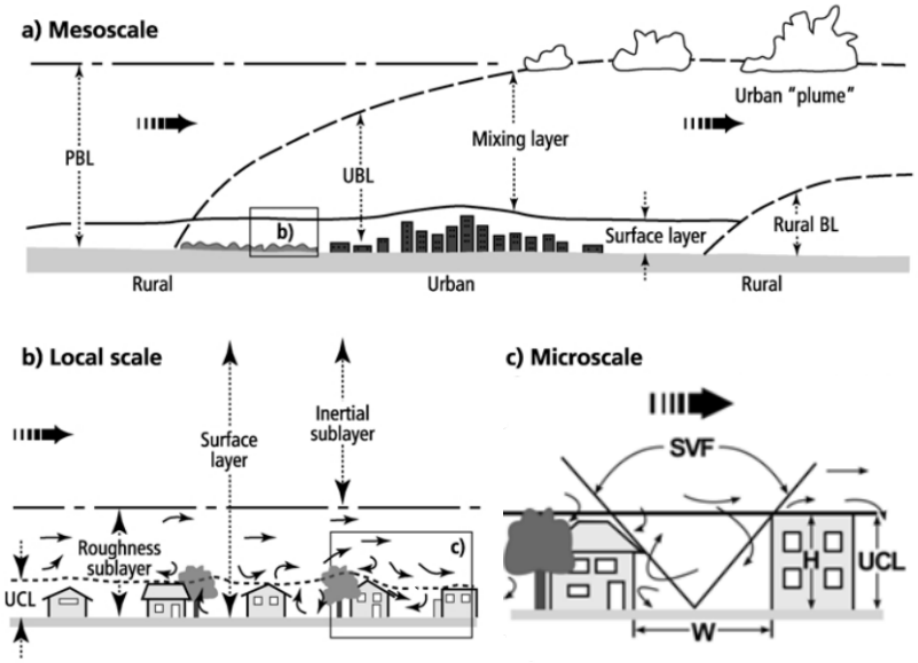

Figure 2.2: Different scales and layers within the PBL (SVF=Sky-view factor), adapted from Száraz (2014); Piringer et al. (2002).

The urban canopy layer (UCL) and the roughness sublayer (RSL) can be separated from the SL in urban boundary layers (Stull, 1988; Száraz, 2014). These structure of these sublayers is represented in Figure 2.2. UCL is located within the RSL and covers the layer between the rooftops and the ground. This layer has strong turbulence due to it being in closest proximity to the individual roughness elements such as buildings and trees. This layer also experiences the strongest effect of the emitted longwave radiation by the anthropogenic surfaces, which can contribute to the formation of local heat pockets (Park et al., 2017; Száraz, 2014). The RSL is differs from the IS in the way that the buildings still affect the flow properties individually, while in the IS the turbulent mixing has started to be great enough that the effect of a single roughness element is not as evident. Further above in the ML this turbulent mixing is large enough that the layer's properties are rather defined by mesoscale processes and the overall effect of the underlying layers.

The wind profile in the SL typically follows a logarithmic shape, with increasing wind speeds higher above the ground (Stull, 1988). In UCLs however, the starting height for this profile can be offset from the actual ground level by an amount known as displacement

height, which is typically 2/3 of the mean building height.

2.2 Turbulence

The main reason why the boundary layer differs from the free atmosphere is turbulence. Turbulence consists of three-dimensional swirling vortices, called eddies (Stull, 1988). The size range of these eddies is limited in the larger scale by the depth of the boundary layer, and in microscales by the molecular viscous forces which turn the kinetic energy into heat energy (Stull, 1988; Oke, 1988). This process of energy transfer and eventual dissipation from larger to smaller scales is called the energy cascade. Turbulence is dissipative and the eddies get their energy directly from the mean flow. Turbulence transports mass, momentum and energy and is also a great mixer of these quantities, which is why the closest layer of the atmosphere to the ground is often described as a constant flux layer due to the amount of mixing by the eddies (Stull, 1988).

2.2.1 Navier-Stokes and incompressible flow

One of the basic equations used to describe fluid flow in the atmosphere is the continuity equation (2.1), which describes flow incompressibility (Stull, 1988). This form suggests that mass is conserved and because there is no change in volume, density effectively stays the same. This combined with the Navier-Stokes equation (2.2) for incompressible fluids decribes the flow conditions in a turbulent atmosphere. Depending on the studied scale, some terms can be left out if they become negligible, such as the coriolis term when dealing with processes in the PBL.

$$\frac{\partial u_j}{\partial x_j} = 0 \tag{2.1}$$

$$\underbrace{\frac{\partial u_i}{\partial t}}_{\text{Momentum storage}} + \overbrace{u_j \frac{\partial u_i}{\partial x_j}}^{\text{Advection}} = \underbrace{-\delta_{ij} g}_{\text{Gravity}} + \overbrace{f_c \varepsilon_{ijk} u_j}^{\text{Coriolis force}} \underbrace{-\frac{1}{\rho}\frac{\partial p}{\partial x_i}}_{\text{Pressure gradient}} + \overbrace{\nu \frac{\partial^2 u_i}{\partial {x_j}^2}}^{\text{Viscous stress}} \tag{2.2}$$

where $f_c = 2\Omega sin(\psi)$ is the coriolis parameter, in which Ω is the angular velocity of the Earth and ψ is latitude. Other variables include air density ρ, gravitational acceleration g, pressure p and kinematic viscosity ν. δ_{i3} is called the Kronecker delta:

$$\delta_{ij} = \begin{cases} 1, & \text{if } i = j, \\ 0, & \text{if } i \neq j. \end{cases} \tag{2.3}$$

Finally, ε_{ijk} is called the Levi-Civita symbol:

$$\varepsilon_{ijk} = \begin{cases} 1, & \text{if any of } ijk = [123, 231, 312] \\ -1, & \text{if any of } ijk = [132, 213, 321] \\ 0, & \text{if contains any of } [ij, ik, jk] = [11, 22, 33] \end{cases} \tag{2.4}$$

2.2.2 Covariance and fluxes

When studying meteorological variables over longer time periods, two components are identified (Stull, 1988). Fluid flow can be described as a sum of these components, the mean flow ($\overline{A}$) and the turbulent fluctuations (A'):

$$A = \overline{A} + A', \tag{2.5}$$

where A can be any time series of a variable. Here the mean of the turbulent part ($\overline{A'}$) is by definition 0, because the positive and negative deviations from the mean cancel each other out over long time periods. This concept of separating the mean and turbulent part is called the Reynolds decomposition. When two variables are multiplied together with this decomposition into the mean and turbulent parts taken into account, all that remains after Reynolds averaging are the multiple of the means and their turbulent parts.

$$\overline{(A \times B)} = \overline{AB} + \overline{A'B'}, \tag{2.6}$$

where A and B can be two different variables such as one wind component and temperature, or even the same variable multiplied by itself. In the former case the second

term on the right is called the covariance between the two variables, and with the same variable twice it is called variance (covariance with itself). This covariance term describes the relationship between the two variables. When one of the terms is the vertical wind component w and the term is positive, there is a flux upward and vice versa for a negative covariance. These nonlinear covariances also describe the interaction between the surface and the atmosphere and are especially imporant in the boundary layer, where the magnitude of turbulent fluctuations is the greatest (Stull, 1988).

The main fluxes associated with the interaction processes between the atmosphere and the surface have to do with the transfer of heat, momentum and moisture. The fluxes describing these interactions are called the sensible heat flux H, momentum flux τ, latent heat flux LE and the ground heat flux G.

$$\begin{aligned} H &= \rho C_p \overline{w'\theta'} \\ \tau &= \rho \sqrt{\overline{u'w'}^2 + \overline{v'w'}^2} \\ LE &= \rho L_v \overline{w'q'}, \end{aligned} \tag{2.7}$$

where C_p is the dry air specific heat capacity, L_v is the latent heat of vaporization and q' is the turbulent part of the specific humidity. The terms in equation 2.7 are called the eddy covariance fluxes, because they are represented through the covariances rather than in the bulk flux from, which for example use wind speed at the surface and 10 meters above ground and takes their difference (Stull, 1988).

2.2.3 Turbulent kinetic energy

Turbulent kinetic energy (TKE $= \frac{1}{2}(\overline{u'^2} + \overline{v'^2} + \overline{w'^2})$) describes the amount of energy within the swirling eddies associated with turbulent flow, and is often used to assess how turbulent the atmosphere is at a given time. TKE consist of the horizontal wind variances u'^2 and v'^2 and the vertical wind variance w'^2. The change in time or tendency of the mean turbulent kinetic energy ($\overline{e}$) is a balance of the production, transport and dissipation

terms:

$$\underbrace{\frac{\partial \overline{e}}{\partial t}}_{\text{storage}} = \underbrace{\frac{g}{\overline{\theta}_v}(\overline{w'\Theta_v{}'})}_{\text{thermal production}} \overbrace{-\overline{u'w'}\frac{\partial \overline{U}}{\partial z}}^{\text{mechanical production}} \underbrace{-\frac{\partial(\overline{w'e})}{\partial z}}_{\text{turbulent transport}} \overbrace{-\frac{1}{\overline{\rho}}\frac{\partial(\overline{w'p'})}{\partial z}}^{\text{pressure correlation}} \underbrace{-\varepsilon}_{\text{dissipation}}, \quad (2.8)$$

where g is acceleration due to gravity, $\overline{\theta_v}$ is the mean virtual potential temperature, p' is the perturbation pressure and ε is dissipation of turbulence. Here the horizontal axis is aligned with the mean wind ($\overline{U}$) such that we only end up with one term in the mechanical production of turbulence (Stull, 1988). The two most important terms for this thesis are the first two production terms, especially the thermal production of TKE. Mechanical production derives from the surface roughness, when individual roughness elements such as buildings, trees and changes in orography interfere with the mean flow, which induces vortices and therefore turbulence. Thermal production of turbulence occurs when localized regions of warm air rise up in convective currents know as thermals, which are also the largest eddies in an urban boundary layer. Due to the last term, turbulence is not a conserved quantity, meaning that it tends to decrease with time by dissipation to heat unless generated by the production terms or transported from elsewhere.

2.3 Characteristics of urban flow

Buildings and vehicles also provide their own source of heat output as anthropogenic sources, which mix with the air and result in a boundary layer with different properties than a rural one (Oke, 1988; Stull, 1988). The roughness of the urban surface elements leads to localized areas of slower wind speeds compared to the undisturbed main flow, which causes velocity gradients to form. The existence of disturbed flow in the wake of buildings and trees means that there is drag and therefore pressure perturbations downwind. The resulting resistance on the mean flow leads to stress forces, which transfer momentum from higher altitudes towards the ground (Oke, 1987). Mechanically produced eddies have a similar scale in size as the object which created it, whereas rising thermals

resulting from convective processes have scales up to the depth of the BL.

2.3.1 Effect of buildings

The effect of the individual elements themselves on flow conditions depend on their physical properties such as shape and permeability. Buildings are impermeable unlike trees, and have sharp edges where the sudden change in resistance can more easily induce the formation of vortices (Oke, 1987). A number often used to estimate the flow patterns within street canyons is the aspect ratio H/W, where H is the height of the building canopy and W is the width of the canyon and therefore the spacing between individual buildings. The three main types of canyon flow regimes are represented in Figure 2.3. Each flow regime has a different effect on the resulting vortex structure and flow conditions, with an increase in the decoupling of the vortex and main flow as the street canyon gets narrower. This vortex structure is mainly present with cross-canyon flow, meaning that the direction of the mean wind is perpendicular (at a 90° angle) with the street canyon. If the wind direction changes, the resulting flow can first become helical in structure as a stretched vortex along the canyon. As the direction changes further and the flow is along the canyon, part of the flow separates and goes around the buildings, but some is more tightly packed and forced to flow along the canyon in a process called channeling.

2.3.2 Radiative effects

While buildings and trees have an effect on flow, they also obstruct the total received sunlight for a given area, determined locally by the sky-view factor (Park et al., 2017; Oke, 1987). Figure 2.4 depicts this relationship between building density and the amount of sky or adjacent urban surfaces that is visible at a given point.

Most important factors in determining the radiative transfer processes in a local city environment include the aspect ratio and the orientation of the canyons (Oke, 1987). Depending on the material, angle, albedo and heat storage properties, two surfaces under

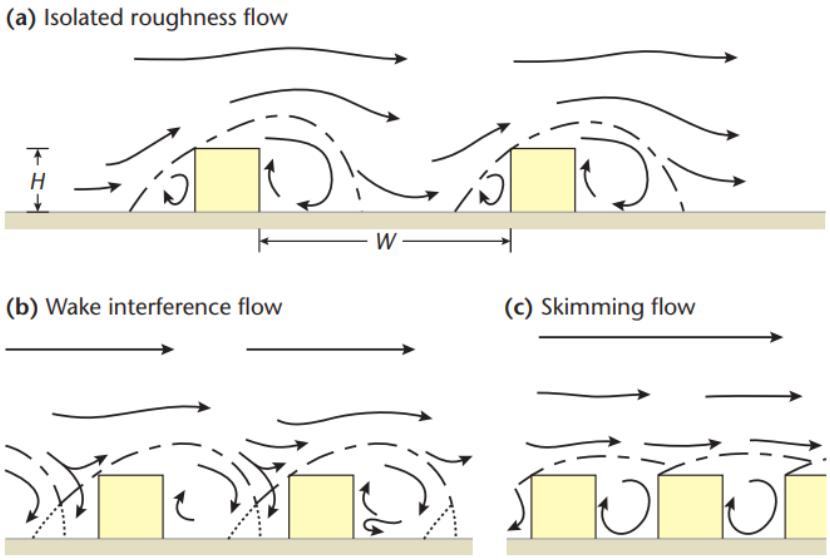

Figure 2.3: Different flow regimes depending on the aspect ratio (Oke, 1987).

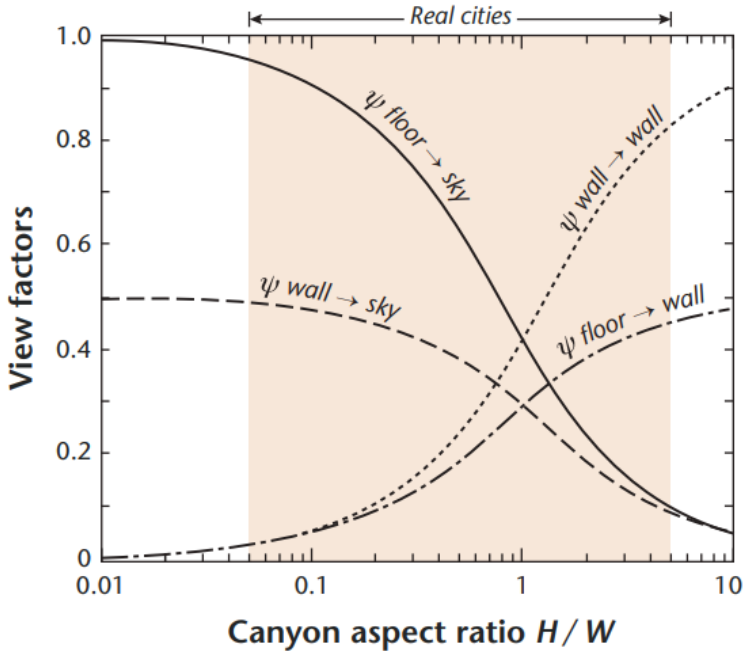

Figure 2.4: Relationship between the view factors (ψ) of urban facets and the canyon aspect ratio (Oke, 1987).

the same initial conditions can have very different behavior in terms of their thermal conditions. Sunlight (shortwave radiation) coming at a small angle results in shadows, which means that areas left without this direct energy input can experience cooling, whereas surrounding walls and roofs experience further warming. There is a constant

interplay between the two types of radiation involved; longwave and shortwave radiation. Streets with large aspect ratios have all the urban surfaces like the floor and walls in close proximity to each other, which increases the amount of reflections in the canyon and minimizes longwave radiative loss. All these radiative effects combined can strengthen horizontal and vertical temperature gradients, which leads to different stability conditions and therefore more complicated flow patterns. A direct example of radiative effects on local flow conditions is the cross-canyon vortex discussed in section 2.3.1. Orientation and shading can lead to one side experiencing direct warming due to incoming shortwave radiation, which enables the surface to warm up quickly to higher temperatures than a shaded similar wall. This leads to microthermals within close vicinity of the sunlit wall, which can either inhibit or enhance the street vortex, depending on if the direction of induced vertical motion is in the same direction as the topographically forced vortex (Oke, 1987; Iacono et al., 2000).

2.4 Large-Eddy Simulation (LES)

LES (Large-Eddy Simulation) is based on separating the different scales in turbulence and only resolving the ones which are most relevant for sufficiently accurate modeling, while parameterizing the smallest scales (Maronga et al., 2020; Tominaga and Stathopoulos, 2010; Argyropoulos and Markatos, 2015). The three main types of computational fluid dynamics modeling methods are called RANS (Reynolds Averaged Navier-Stokes), LES and DNS (Direct Numerical Simulation). They differ essentially in the scales they directly resolve or parameterize. RANS deals with temporal averages, hence it is computationally cost effective, but at a loss of accuracy when the smallest scales are not captured by the longer averaged time periods (Hooff et al., 2017). DNS is at the other end of this spectrum, where all of the scales are resolved. This has a high computational cost, and applying it to a large city environment with scales reaching just a few millimeters and centimeters, is mostly reserved for modeling flow for example within a single apartment or other high resolution phenomena requiring direct modeling of these scales (Argyropoulos

and Markatos, 2015). LES is essentially the middle ground between these two extremes, by resolving the most relevant scales, meaning the ones which contain most of the energy and then parameterizing the smallest scales (Maronga et al., 2020). In general, LES models solve the three-dimensional Navier-Stokes equation for fluid flow, temperature, humidity and other scalars such as pollutants. The parameterization of small scales is done through the relationship between small eddies and properties of the main flow, like the vertical and horizontal gradients. The largest scales have an input of energy, which is transfered to smaller and smaller scales in the inertial range, eventually dissipating into heat due to viscous forces in the dissipation range. LES covers roughly all the eddy sizes until the start of this last dissipation range. Models such as PALM are able to directly resolve phenomena larger than the smallest grid cell size, but for small scale phenomena parameterization is required through the use of the subgrid-scale model (SGS).

3. Methods

As turbulent processes reach into the microscales, the computational resources and methods required to accurately describe them becomes more important and difficult. From the different modeling methods described earlier, LES is the most suitable choice due to both its cost effectiveness and that the main focus is on small scale processes, which are mostly found in the UCL (Tominaga and Stathopoulos, 2010).

3.1 PALM

The model used in this thesis to simulate turbulent processes is called PALM, which is a long-used LES model to study atmospheric and oceanic boundary layers flow and dynamics (Maronga et al., 2020). PALM has the option to utilize many modules that handle the interactions between the surface and the atmosphere, such as the land surface model (LSM) and urban surface model (USM) (Gehrke et al., 2020; Resler et al., 2017). A plant canopy model (PCM) is used to model the interaction between vegetation and flow. The modules used depend on the situation and processes that the researchers are interested in. This thesis is mainly focused on radiative processes and the resulting interactions between the atmosphere and surface close to the ground. (Maronga et al., 2020).

3.1.1 Nested runs

Nesting offers a way to simulate large areas while keeping the computational cost low (Hellsten et al., 2021). In order to do this the domain has to be divided into different

nesting domains. The root domain, which covers the entire modeling domain and has the coarsest resolution, is used to feed the boundary conditions into the smaller domains to ensure that the area of interest does not depend on the boundary conditions. In the domain, the spatial resolution has to be high enough to capture largest turbulent structures. In nesting, smaller subdomains with a higher resolution can be defined within the root domain. These smaller subdomains are called parents and they can be divided into further subdomains called child domains. This division and assigning of smaller subdomains is called nesting, and the interaction between the outer and inner domains can be assigned to be two-way or one-way nesting, with the difference being the directions that information is shared in.

3.1.2 Land-Surface Model (LSM)

For land-surfaces, such as vegetation, pavement and soil, the interaction between the surface and atmosphere can be modelled using the land-surface module LSM embedded in PALM (Gehrke et al., 2020). It contains a solver for the energy balance (3.1) over each surface. An additional soil layer is defined below the surface types. The surface types are categorized into vegetation, pavements or water surfaces. All of them are further divided into more classes. Each class has its own physical properties. Soils have different porosities which affect moisture and thermal transport, pavements have different heat capacities and albedos which affect how much heat is stored in the ground, and vegetation surfaces have information about their thermal properties and the leaf area index. LSM uses this classification to calculate the the energy balance based on received energy from incoming radiation. The radiation can be directly emitted or indirectly reflected longwave radiation from surrounding buildings or direct and diffuse shortwave radiation from the sun. The energy balance between the surface and the atmosphere is solved from the equation:

$$\frac{dT_0}{dt}C_0 = R_{net} - H - LE - G, \tag{3.1}$$

where T_0 (K) and C_0 ($\frac{\mathrm{J}}{\mathrm{K\ m^2}}$) describe the radiative temperature and heat capacity of the modeled surface and $G(\frac{\mathrm{W}}{\mathrm{m^2}})$ is the ground heat flux, which describes the heat transfer between the atmosphere and the top soil layer. The positive direction is defined differently between R_{net} and rest of the terms, with positive direction downwards in R_{net} and upwards in other terms.

The fluxes in (2.7) and the ground heat flux in (3.1) are parameterized in PALM as follows:

$$\begin{aligned} H &= -\rho C_p \frac{1}{r_a}(\overline{\theta}_{mo} - \theta_0) \\ LE &= -\rho L_v \frac{1}{r_a + r_s}(\overline{q}_{v,mo} - q_{v,sat}(T_0)) \\ G &= \Lambda(T_0 - T_{soil,1}), \end{aligned} \tag{3.2}$$

where r_a is the aerodynamic resistance, $\overline{\theta}_{mo}$ is the potential temperature at the height where MOST is applied, θ_0 is potential temperature at the surface, r_s is the surface resistance, $q_{v,mo}$ is the water vapor mixing ratio at the height where MOST is applied, $q_{v,sat}$ is the saturated water vapor mixing ratio, Λ is the total thermal conductivity between the skin layer and the top soil layer, T_0 is the radiative surface temperature and $T_{soil,1}$ is the temperature of the top soil layer (Gehrke et al., 2020).

3.1.3 Urban Surface Model (USM)

An urban surface model is implemented in PALM for buildings (Resler et al., 2017; Maronga et al., 2020). The model contains an energy solver for the atmosphere-surface interaction, similarly as in the land-surface model for ground surfaces (3.1). This energy solver calculates the skin-surface temperature and near surface turbulent fluxes, such as heat conduction flux through the material and sensible heat flux between the surface and air. USM receives radiation input with varying complexity depending on the used radiation scheme, and this information is then used to calculate radiative transfer within the urban canopy. Buildings are treated as impermeable and radiation is able to reflect from these surfaces multiple times, with a portion being absorbed each time to the respective reflective surface. Trees with their varying leaf area densities are treated as

semi-permeable. An additional indoor model can be used, which takes into account heat exchange between the indoor and outdoor areas of buildings (Pfafferott et al., 2020).

3.1.4 Radiation Model RRTMG

Modules such as Urban Surface Model (USM) and Land-Surface Model (LSM) are all a embedded in PALM, meaning that no separate installation steps are required for them (PALM, 2021). RRTMG (Rapid Radiative Transfer Model for Global models) on the other hand is implemented as an external library in PALM (Salim et al., 2020). RRTMG takes in information about the time of day and coordinates, which it then uses to calculate incoming solar radiation to be fed into the radiation scheme of USM and LSM. It is capable of calculating multiple reflections, diffuse radiation and absorbed radiation on different surfaces. Sky-view factors (figure 3.1) are calculated at each radiation timestep and on both vertical and horizontal grid points (Salim et al., 2020).

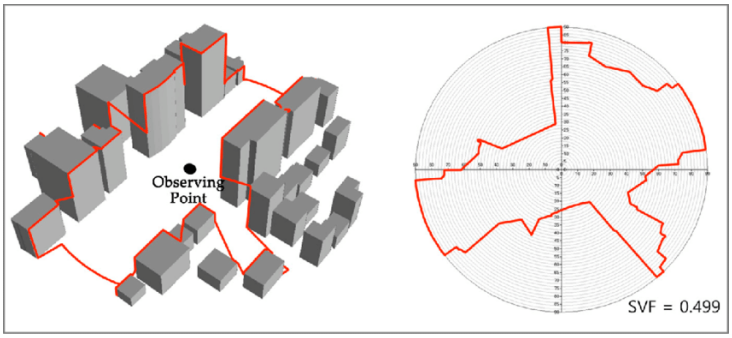

Figure 3.1: Visual representation of the sky-view factor (Park et al., 2017).

A process called raytracing is used, where rays are cast from each surface point and then checked for collisions to get an estimate of how large part of the sky is visible. This is important because it directly relates to how much shortwave radiation a specific surface receives during the run. This is not the only source of radiation however, as narrow street canyons of small view factors have buildings and therefore sources of longwave radiation closer to each other (Park et al., 2017).

3.2 Study site

The area of interest in this study is Mäkelänkatu region in Helsinki, Finland, on the 9th of June, 2017 between 07:00 - 09:15 UTC+3 (Kurppa et al., 2020b). The area shown in figure 3.3 covers the child domain, which has a Local Climate Zone classification of open midrise (LCZ 5) according to the original classification described in Stewart and Oke (2012). The building fraction is 25%, impervious surfaces cover in total 60% of the domain and vegetation covers 40% of the domain. The mean building height is 13.7 meters. The chosen simulation area surrounds an HSY (Helsinki Region Service Authority) measurement site, which is why this area is the center of the domain. Statistical regions 3.2 are areas of special interest in the modeling domain with higher temporal resolutions and have to be manually chosen cell by cell in the source code files. This property makes

Figure 3.2: Child domain with two statistical regions (SR) the Sun's path during the main run

them different from masks, which are subregions of the modeling domain with specific

output that are directly initialized in the input files, without need to modify any code. The statistical regions chosen in the parent and child domains are representations of the HSY measurement campaign locations. The dimensions of the canyon were measured at the location of a measurement container discussed in Kurppa et al. (2020a,b). The height of the canyon is 19 meters on the southwestern side and 16 meters on the northeastern side. The width of the street is 42 meters, which results in an aspect ratio of $H/W = 0.45$. An aspect ratio between 0.35 and 0.65 suggests wake interference flow to occur within the canyon, which means that the street is not wide enough for the flow to only occur horizontally at one side, but also not narrow enough for a more distinctive canyon vortex to form (Oke, 1987). Further details about the study site are described in Kurppa et al. (2020a).

3.3 Model setup

The modeled area consists of three separate nesting domains (root, parent and child) (figure 3.3) (Kurppa et al., 2020b). The root domain has 768 x 768 horizontal cells with 9 meter resolution and 80 vertical cells with 6 meter resolution until a height of 300 meters, after which the grid cells are stretched to increase the domain height without increasing the overall cell amount. This is done because at these altitudes the diameter of eddies is large enough that a coarser resolution is enough for their accurate description. The root domain contains the parent at 768 x 768 x 96 cells each with a resolution of 3 meters. The innermost child domain has 576 x 576 x 144 cells with 1 meter resolution. All three domains are represented in figure 3.3. One-way nesting was chosen, which feeds information about prognostic scalar variables and all three velocity components from the coarser to the finer resolution domains. The solved variables in the inner domains do not affect the outer ones, i.e., the child does not affect the parent and vice versa between the root and the parent (Hellsten et al., 2021).

This case applies information about meteorological forcings such as wind profiles and the pressure field, which are given in a dynamic input file. The dynamic input data

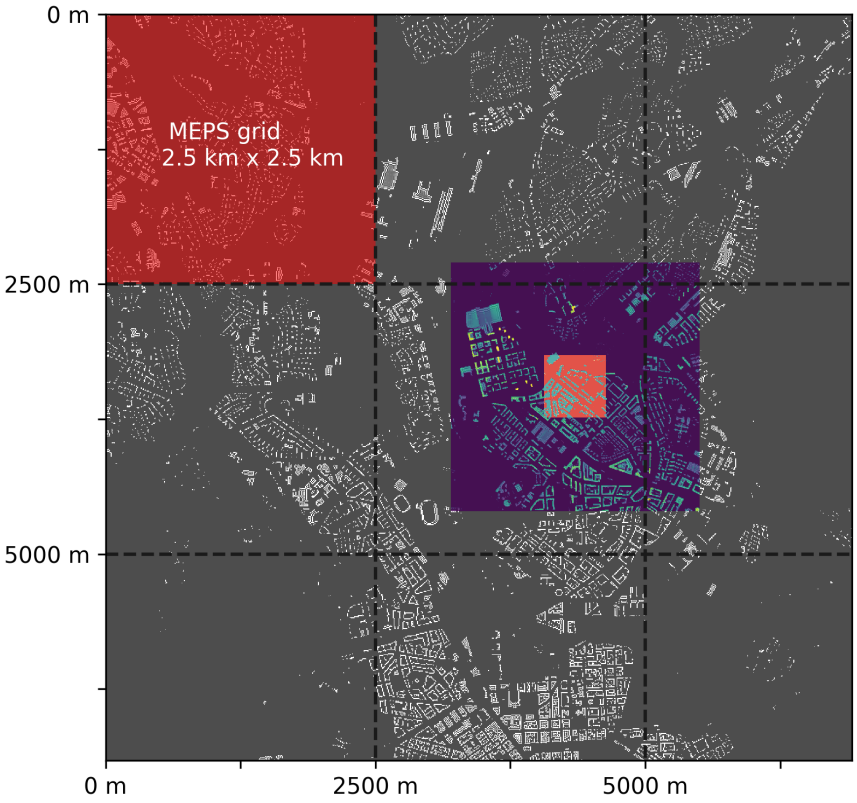

Figure 3.3: Nesting configuration with different domains shown in varying color schemes (Kurppa, 2020b)

are created from the output of the MEPS/HARMONIE weather model (Kurppa et al., 2020b). Other information such as surface types used by the different modules within PALM are given in a static input file (Strömberg and Auvinen, 2020). The surface maps for pavement, vegetation, building and water types and the LiDar topography dataset are obtained from open access land-use maps from Helsinki Region Infoshare (HRI, 2018) and Helsinki Region Environmental Services Authority (HSY, 2017). Soil information was retrieved from the national land survey of Finland GTK (2018). Due to the multiple sources there was some overlap in the raw data between different map layers, hence some filtering and prioritizing of the most accurate maps had to be done for a sufficient end product (Strömberg and Auvinen, 2020).

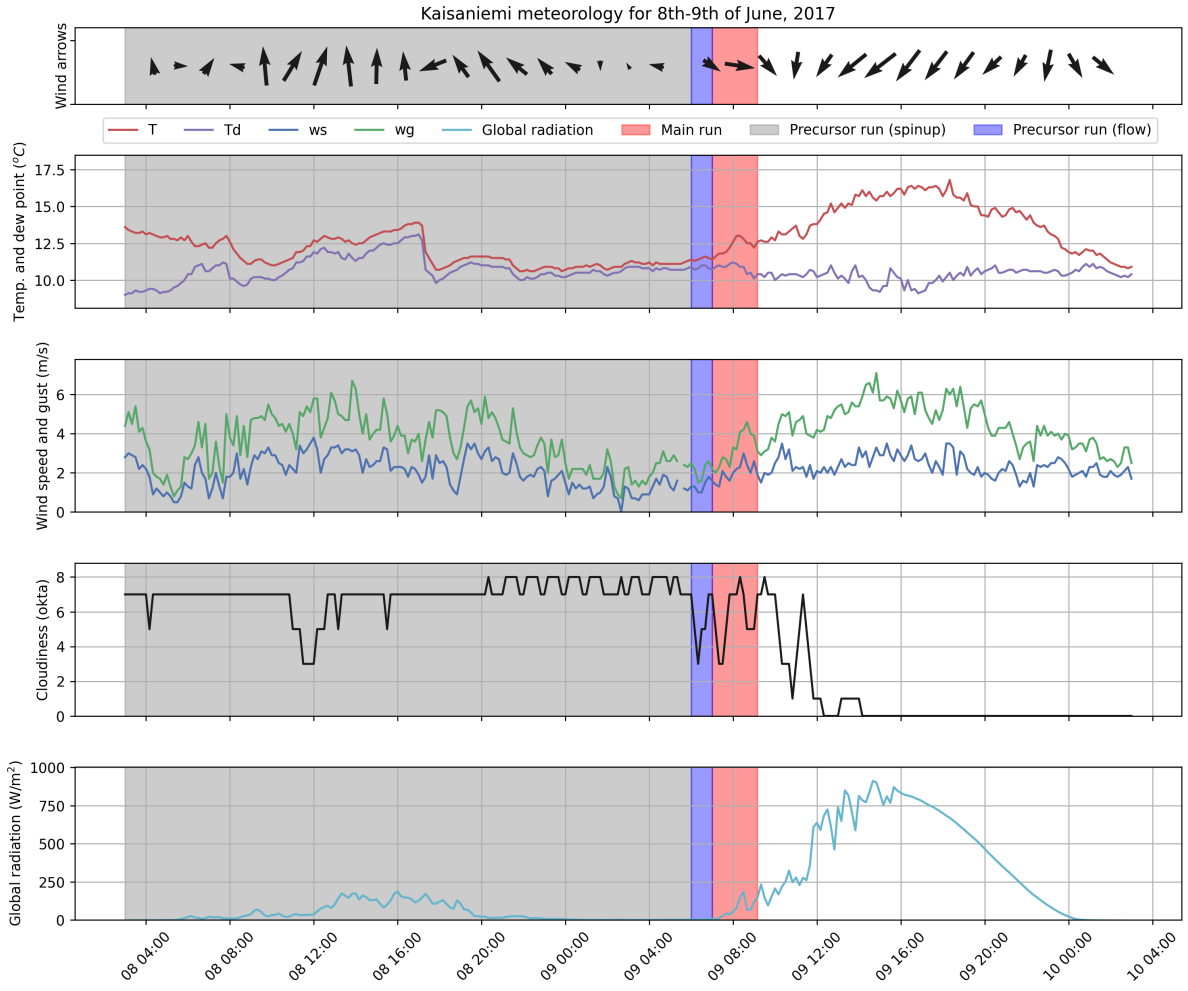

Figure 3.4: Meteorology in Kaisaniemi during the simulated time period at local time (UTC+3) (FMI, 2017)

The precursor run to adjust the flow and surface properties in the model simulation has to be given the magnitude of the mean and variation of the air temperature during the spin-up, which were calculated from FMI (Finnish Meteorological Institute) data from the day prior to our simulation time (figure 3.4). Meteorology during the full simulation period (precursor + main) is shown in figure 3.4 with differently colored shading. The blue and red shaded areas are the same time periods for both runs, with a one hour precursor run for flow and then a 2 hour and 15 minutes long main run. The only difference in length is the additional 24 hour spin-up period (grey shading), which is only for RRTMG On (see section 3.4). There is a contrast between the two days in terms of wind direction, air temperatures and the amount of incoming solar radiation. The day prior to the simulation

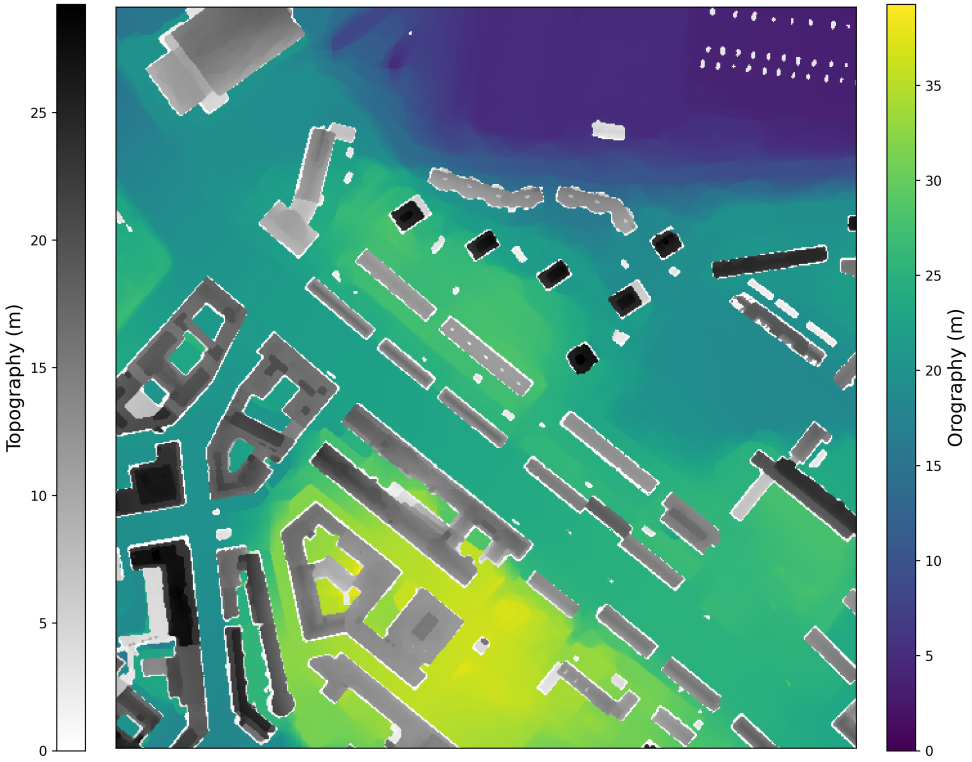

Figure 3.5: Terrain around Mäkelänkatu.

period was a cloudy day with low winds, reaching only just shy of $4\frac{\mathrm{m}}{\mathrm{s}}$. The cloudiness also lead to less incoming sunlight, which is visible as a smaller magnitude in the diurnal cycle of global radiation. The air temperature remained nearly constant, averaging at 12.5°C for the previous day. The last hour of the precursor run showed some signs of breaking clouds and already similar incoming radiation at 8 (UTC+3) than what was received at 16 on the previous day. The main run simulation period was calm with winds close to $2\frac{\mathrm{m}}{\mathrm{s}}$. The wind is coming from the south on the 8th, but turns to northeasterly winds during the 9th. The change in wind direction from the west towards northerly winds is starting to show during the time of the main run.

3.4 Model runs

There are two model runs discussed in this thesis. One of them, called RRTMG Off, is based on runs made in Kurppa et al. (2020b). The other run is called RRTMG On, and it requires special attention due to included radiation module, RRTMG. While RRTMG Off only needs an initializing precursor run of 1 hour to initialize the flow field. RRTMG On requires an additional spin-up period of preferably 86400 seconds as described in Krč et al. (2021).

3.4.1 Initialization

Before the main model run, a precursor run needs to be made to warm urban surfaces to realistic temperatures and to initialize flow and turbulence (Salim et al., 2020). The precursor run consists of a spin-up period of 86400 seconds, which solves for radiative transfer with a timestep of 60 seconds. The run is given the mean near surface potential temperature (285.15 K) and its amplitude (3 K), but the modeled temperatures also depend on the coordinates of the modelling domain and time of day, which affect how much shortwave radiation reaches the surfaces. After the spin-up period is done the flow is simulated for 3600 seconds to both introduce turbulence in the domain and initialize the flow field (Kurppa et al., 2020b).

3.4.2 Main run

All the domains are initialized with restart data written at the end of the precursor run. The main run, which solves for radiation and flow, was run for 11700 seconds between 7:00-9:15 UTC+3. (Kurppa, 2020a; Kurppa et al., 2020b). The mean wind is from the west and it turns slightly towards northeast during the second half of the run. There are two statistical regions chosen for more output data. SR1 at the north side of a measurement container in the middle of Mäkelänkatu close to the southern building wall and SR2 directly on the other side of the street.

3.5 Data output and post-processing

PALM offers a wide variety of output variables, which include profiles, time series, vertical and horizontal cross sections. Most of these, also used in both RRTMG On and RRTMG Off, require additional processing. High temporal resolution can often be computationally expensive, which is why specific sections called masks can be saved with a higher output timestepping compared to the whole child domain. The dimensions of the masks and the saved output have to be individually chosen based on which areas are most interesting. One of those output areas (area 1) is a 461 m × 461 m subdomain, which focuses more on the central part of the child. The main benefit of this area is to exclude the borders of the child domain, which are not needed to get data of the Mäkelänkatu street canyon. There are also statistical regions available, which include spatially averaged profiles and their time series at each height level. In the Mäkelänkatu street canyon there are two statistical regions, both of which are spatially averaged over a 5 m × 5 m area. An additional reference area at the edge of a gravel football field is located in the northern part of the child. Wind directions are averaged for three time periods, which are all calculated upwards from 60 meters above the ground to avoid any disturbances due to channeling or from the tallest buildings.

3.5.1 Grid and coordinate rotation

One of the most interesting areas of mask 1 is Mäkelänkatu itself. In order to calculate the mean canyon cross section along the street, a grid and coordinate rotation has to be made since Mäkelänkatu is not aligned in the North-South direction. Figure 3.2 shows in red shading the area for which a rotation of 51° has to be done to align the y-axis with Mäkelänkatu. This allows for taking the mean along the street for the canyon vortex and provides an overall understanding of the circulation pattern within the canyon. The 144 meter strip takes into account both sides of the canyon and follows the terrain as shown

in figure 3.5.

After the 51° grid rotation, both horizontal wind components require a coordinate rotation such that Mäkelänkatu is aligned with the y-axis, which can be calculated in matrix form as follows:

$$\begin{bmatrix} u_r \\ v_r \end{bmatrix} = \begin{bmatrix} cos(\theta) & sin(\theta) & 0 \\ -sin(\theta) & cos(\theta) & 0 \end{bmatrix} \begin{bmatrix} u \\ v \end{bmatrix} = \begin{bmatrix} u \times cos(\theta) + v \times sin(\theta) \\ v \times cos(\theta) - u \times sin(\theta) \end{bmatrix} \tag{3.3}$$

where u_r, v_r and w_r are the now rotated wind components and θ is the angle between the street canyon and the true North.

3.5.2 TKE production terms

In addition to the rotation of the street canyon, the production terms in the TKE equation (2.8) have to be calculated from the profiles of the fluxes. The momentum flux ($\rho\overline{u'w'}$) is converted to the mechanical production term ($-\overline{u'w'}\frac{\partial\overline{u}}{\partial z} - \overline{v'w'}\frac{\partial\overline{v}}{\partial z}$). The momentum flux is calculated with both horizontal wind component terms in the equation as the axis is not aligned with the mean wind. The vertical gradients for both horizontal wind components are calculated from the profiles of the wind components using Python's NumPy package and its gradient tool, which uses a second order accurate central differences to obtain the gradient at each height (Harris et al., 2020). The profile data are evenly spaced at one meter intervals, which is why the standard second order approximation of the previous process can be used. Heat flux ($\rho C_p\overline{w'\theta'}$) is converted to the thermal production term ($\frac{g}{\overline{\theta}}\overline{w'\theta'}$). The required kinematic fluxes (covariances) come in either momentum/heat flux form (2.7) or as covariances depending on whether or not RRTMG is turned on. With RRTMG off the covariances can be directly used in the budget term calculation, but with radiation on they first have to be converted from flux form to covariances (3.4).

$$\overline{u'w'} = \frac{\tau_u}{\rho},\ \overline{v'w'} = \frac{\tau_v}{\rho},\ \overline{w'\theta'} = \frac{H}{\rho C_p}, \tag{3.4}$$

4. Results and discussion

4.1 Temperature distribution

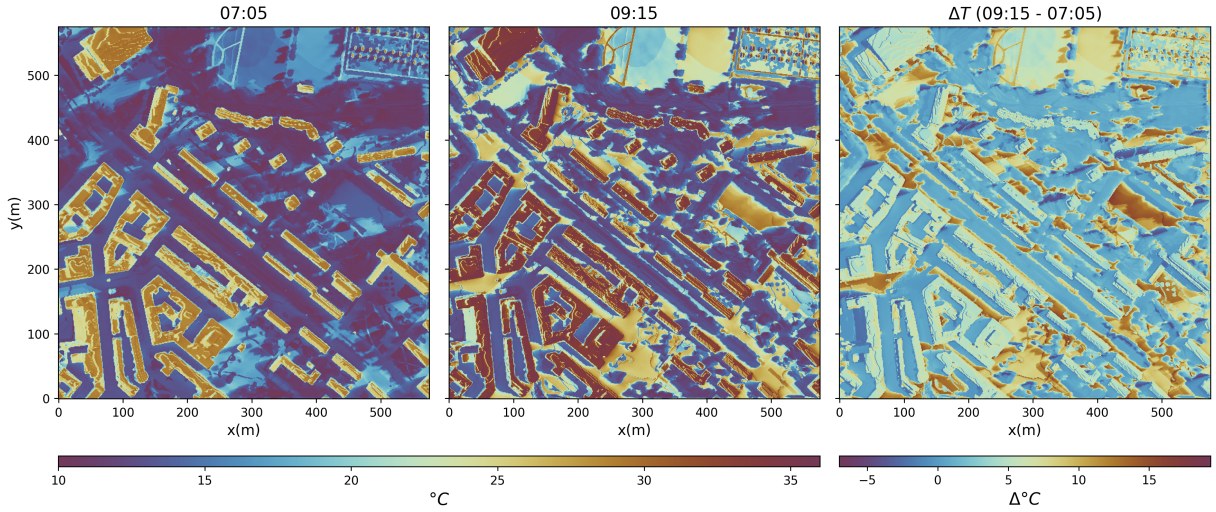

Figure 4.1: Surface temperatures at the start (07:00-07:05) and end (09:10-09:15) of the main run for the child domain and their difference for RRTMG on.

Figure 4.1 shows snapshots of the initial and final five minute average surface temperatures and the overall change during RRTMG On. This information is only available for RRTMG On, as the surface temperature variable is only calculated when radiative processes are taken into account. The areas with the lowest surface temperatures correspond with the location of shadows cast by trees and buildings (Figures 3.3, 4.1). Surfaces containing less moisture such as gravel paths and buildings are both at warmer initial temperatures already at the start of the main run and therefore heat up more compared to vegetative areas. For example the large open football field visible in 4.1 sees a change in surface temperature of between 10 - 15°C compared to the shaded strip at the center of

Mäkelänkatu, which warmed by 1°C during the main run. Other studies such as Gillner et al. (2015) and Tan et al. (2016) also reported a similar decrease of surface temperatures between shaded and exposed areas of 10 - 18 °C. These temperature differences depend on the time of day and SVF. The building roofs have the largest surface temperatures across the domain throughout the simulation. Roofs of tall buildings have large SVFs as they are the tallest structures in the area, which means that they get the largest amount of solar radiation without any obstructions by trees or surrounding buildings. The sun is still very low in the sky early in the morning, which leads to a visible contrast between the heated and shaded areas due to the long shadows caused by varying topography. The buildings in figure 4.1 reached the highest surface temperatures of 36°C at some locations, which are visible in the last timestep of surface temperatures. The areas with the largest surface temperatures, mostly rooftops, did not encounter a large change during the main run since they were already nearing 30°C at the start. The paved surface on the west side of Mäkelänkatu got warmer than the shaded east side, as seen in Figure 4.1 depicted by the warmer colors. The cooling effect of shading can be seen from the overall change in surface temperatures behind individual buildings, but also along the northeastern side of street canyons close to the walls. Due to the RRTMG Off surface temperature data being unavailable, the mean air temperature closest to the ground was used to get an understanding of how much the surface temperatures increased between RRTMG On and RRTMG Off. The results show the closest air temperature (1 meter above the surface) averaged over the main run and mask 1 area to be at 12.5°C (8.6°C) for RRTMG On (Off), which results in an increase of 3.9°C.

Furthermore, this is an early summer morning case and the solar azimuth angle is low, hence at the start of the run solar radiation has not yet reached all the street canyons. Mäkelänkatu is also a wide street at 42 meters across, hence any warming associated with longwave radiation is not as strong compared to narrower street canyons (Park et al., 2017). The walls facing west along Mäkelänkatu are still experiencing cooling from the previous 24 hour precursor run, which can be seen as the narrow strips with a decrease

in surface temperatures in Figure 4.1.

4.2 Flow field

In addition to changes in air temperatures, the radiation scheme also shows a difference in the flow field compared to the RRMTG Off run. Namely, the mean wind direction over the child domain was observed to change when the radiation was included. Similar results have been found in earlier studies (Dimitrova et al., 2009; Qu et al., 2012; Bottillo et al., 2014). The first hour (07:15 - 08:15) mean wind direction for RRTMG On (Off) was 269° (271°) and for the last hour (08:15-9:15) 288° (308°). The averages for the main run (07:15 - 09:15) were 278° (289°) for RRTMG On (Off). The situation with the closest wind direction to cross canyon flow happens during the first hour of RRTMG On. Similarly the direction of mean wind closest to being aligned with the canyon during the latter half of RRTMG Off. During both runs the wind direction was more strongly perpendicular in RRTMG On, which could be a one reason why the canyon vortex is more organized compared to RRTMG Off.

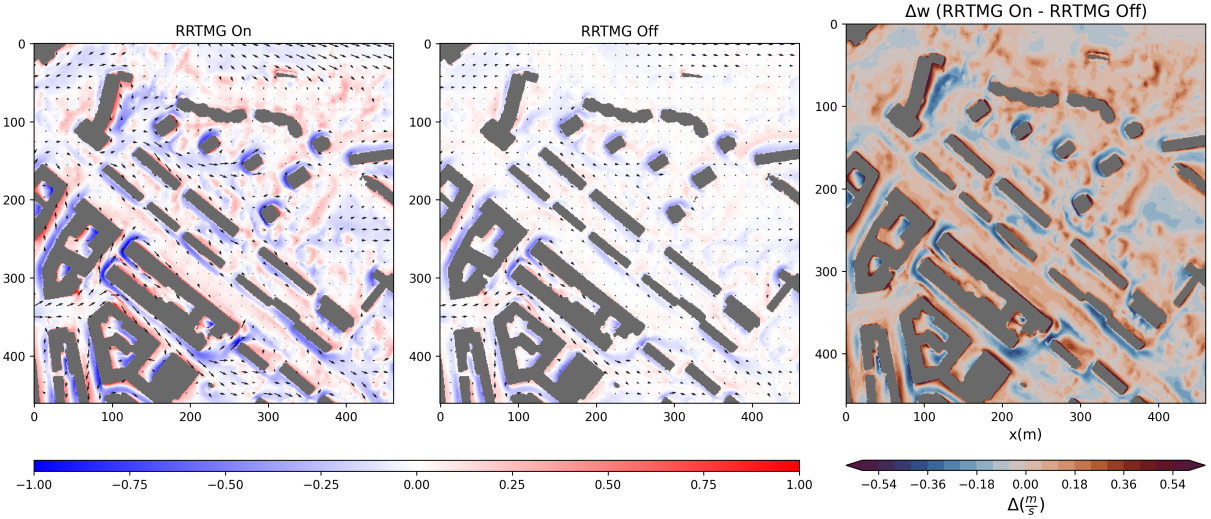

Figure 4.2: Mean vertical motion (color) and horizontal wind speed (arrows) at a height of four meters above ground between 07:15-09:15 for the child domain. The length of the longest arrow to 2 m/s. On the left are plotted the vertical wind speed at 4 meters above ground for the run with radiation interaction included, named RRTMG On. The colors show areas of ascent in red and descent in blue.

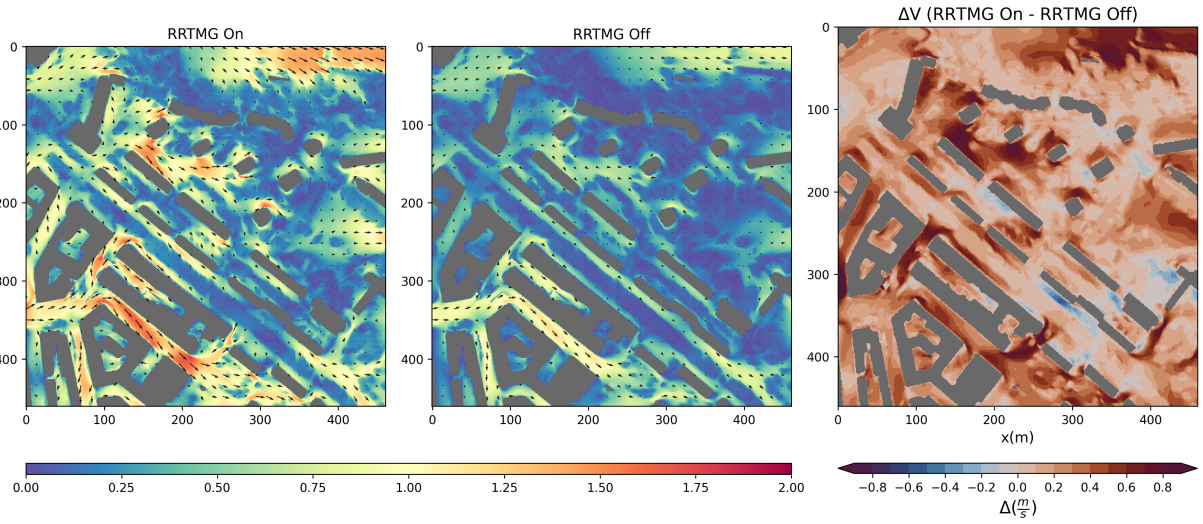

Figure 4.3: Mean horizonal motion between 07:15-09:15 for the child domain four meters above ground. Longest arrow length contributes to 2 m/s

Figures 4.2 and 4.3 show the mean vertical and horizontal flow in and around the Mäkelänkatu street canyon for both RRMTG On and Off runs. Heterogeneous heating due to the solar radiation warms some surfaces more than others, which results in localized areas of ascent compared to cooler, shaded areas (Oke, 1987). This difference in heating also means that opposing areas of convergent and divergent flow form, which consequently strengthens horizontal flow. The inclusion of radiation seems to strengthen the overall flow, while still retaining a similar flow pattern across the domain. Looking at the area mean change in wind speeds, horizontal winds increase by 0.22 $\frac{m}{s}$ and vertical winds strengthen by 0.08 $\frac{\mathrm{m}}{\mathrm{s}}$ in both upward and downward directions. Both in the vertical and horizontal motion the magnitude of the wind components increase while the location of ascending and descending flow regions remain at the same locations.

The forming canyon vortex structure along Mäkelänkatu (figure 3.2) can be seen in figure 4.4, which is calculated for the red shaded portion of the street. Canyon vortices can be seen as dipoles of red and blue colors signaling ascent and descent next to each other on opposite sides of the streets in the xy-cross section (figure 4.2) and the canyon cross section (figure 4.4). RRTMG On shows a stronger canyon vortex than RRTMG Off as it is at an optimal angle with the mean wind, which is flowing from the west, with

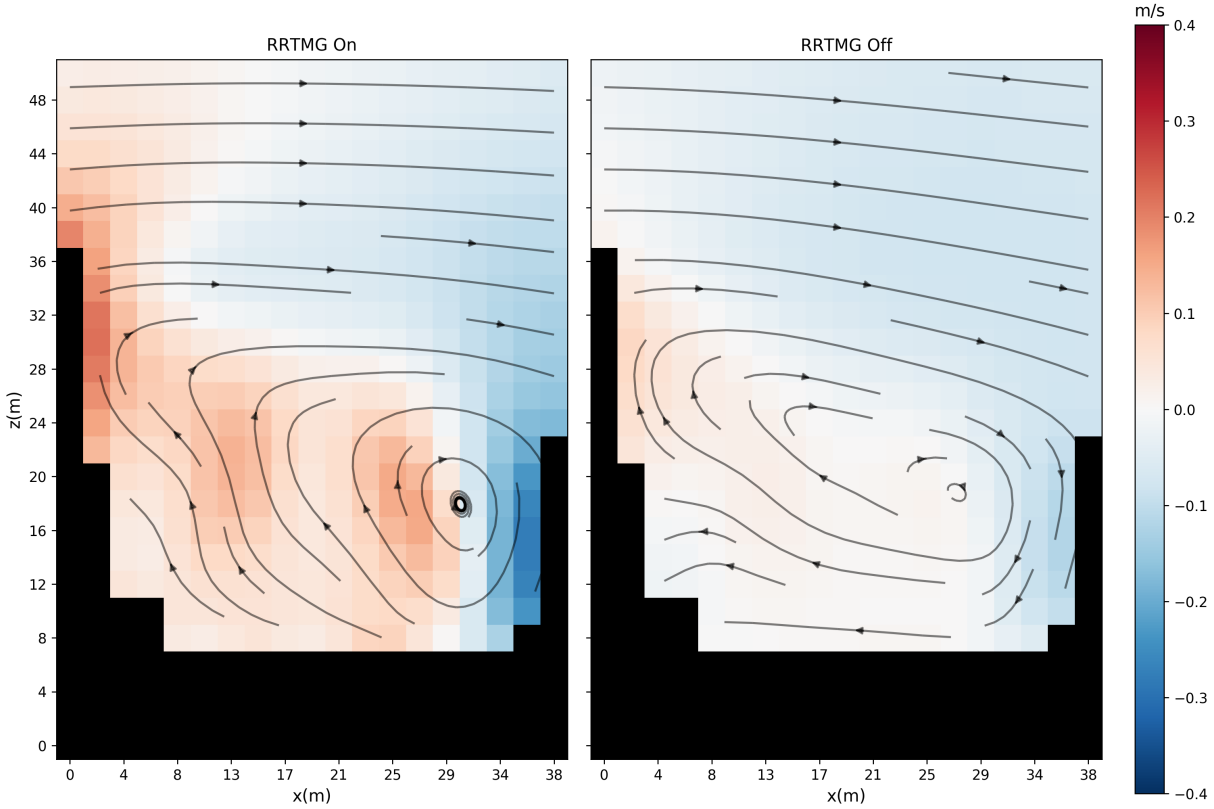

Figure 4.4: Mean vertical wind speed (color) and wind streamplot between 07:15-09:15.

a slight turn towards the north during the latter half of the run (figure 4.2). Overall a warming trend is visible on sun-facing side on the left and a cooling trend along the shaded side, based on the change in surface temperature in figure 4.1. The warming due to changing direction and intensity of the incoming solar radiation eventually leads to the warming spreading more towards the center of the street canyon as the sun rises higher in the sky. This is visible as a more horizontally squeezed vortex in the overall vortex structure (figure 4.4). The magnitude of vertical wind speeds on both sides of the vortex was strengthened by $0.15\frac{\mathrm{m}}{\mathrm{s}}$ on both sides of Mäkelänkatu. A similar change in magnitude was reported by Bottillo et al. (2014), which got a difference in vertical wind of 0.3 m/s on the leeward side of a three-dimensional street canyon. A larger change in the vertical wind speeds could be possible later during the day, as the studied case describes an early morning. The tree crowns are also visible as two areas of stronger updraft in the center of the canyon since they receive and block a lot of the incoming radiation (Salim et al., 2020). Bottillo et al. (2014) also concluded that for low ambient wind conditions of 2 $\frac{\mathrm{m}}{\mathrm{s}}$

the thermal effects on the vortex structure are important, but for an ambient wind of 4 $\frac{\text{m}}{\text{s}}$ the effect is less pronounced.

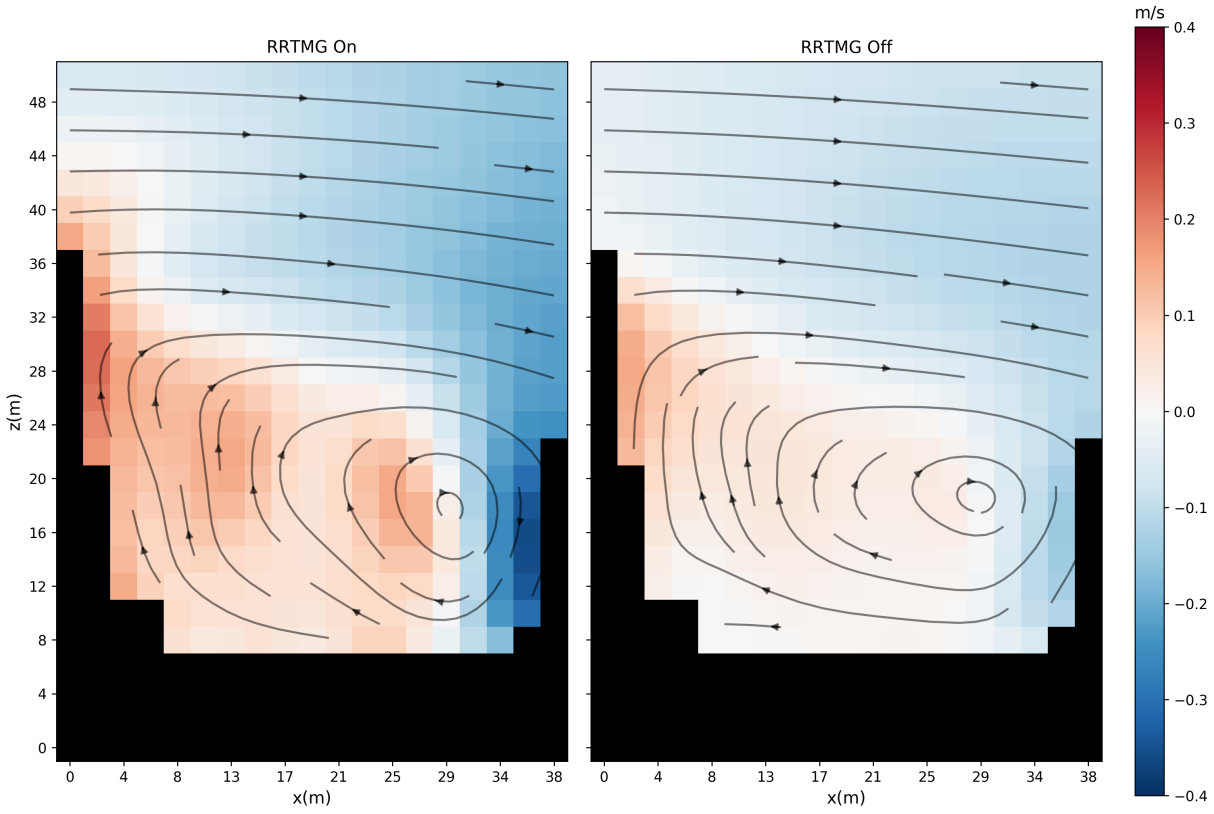

Figure 4.5: Mean vertical wind speed (color) and wind streamplot between 07:15-08:15.

During the first hour the vortex is first formed by the topographical forcing, but even with little solar heating the vertical wind speeds are greater in magnitude, which is visible in Figure 4.5. Due to the wind direction turning more towards flowing along the canyon during the last hour of RRTMG Off, the vortex starts to break down and lose its structure as the center starts to spread out from the canyon (Figure 4.6). The circulation pattern within the canyon is more pronounced in RRTMG On. The forcing of incoming radiation and the warming caused by it seems to act as a restoring force for the canyon in the latter half of the main run, as suggested by Oke (1987). All in all, this effect can also be only a part of the explanation, since the flow had a larger cross canyon component in RRTMG On.

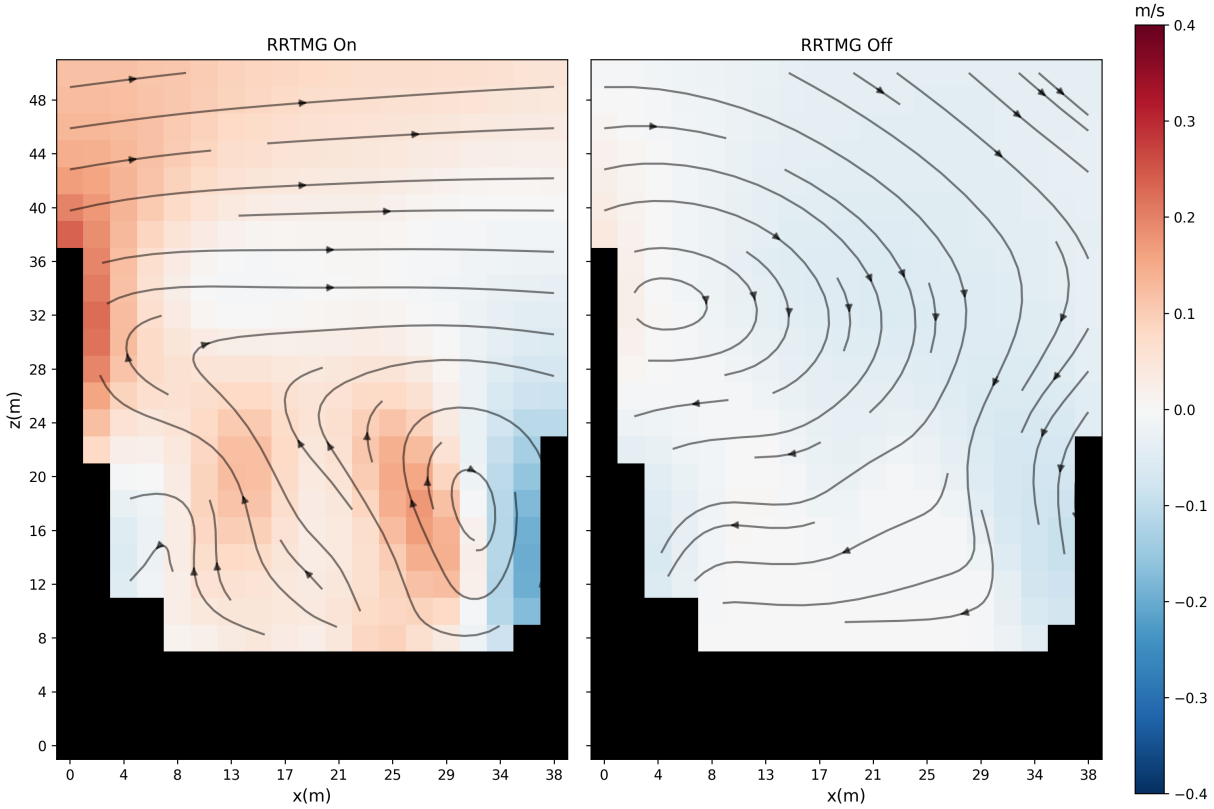

Figure 4.6: Mean vertical wind speed (color) and wind streamplot between 08:15-09:15.

4.3 Vertical profiles

4.3.1 Meteorology

Figure 4.7 shows the mean wind speed, potential temperature and TKE for the full child domain and the two statistical regions (SR1 & SR2, see Figure 3.2) on Mäkelänkatu. The y-axis starts from the first gridpoint above the ground, causing the statistical regions SR1 and SR2 to be 22 meters shorter compared to SR0. The orography in Figure 3.5 shows the height of the starting points of each profile in 4.7. The wind speed increases with height in all cases, whereas the displacement height is visible especially in SR1 as this is the height of the buildings on the windward side. The wind speeds start from zero at the surface and increase as the resistance due to the roughness elements decreases with height. RRTMG On has generally higher wind speeds until a height of about 80 meters above the surface. Averaged over the whole column, the wind horizontal wind speeds increased by only 1%

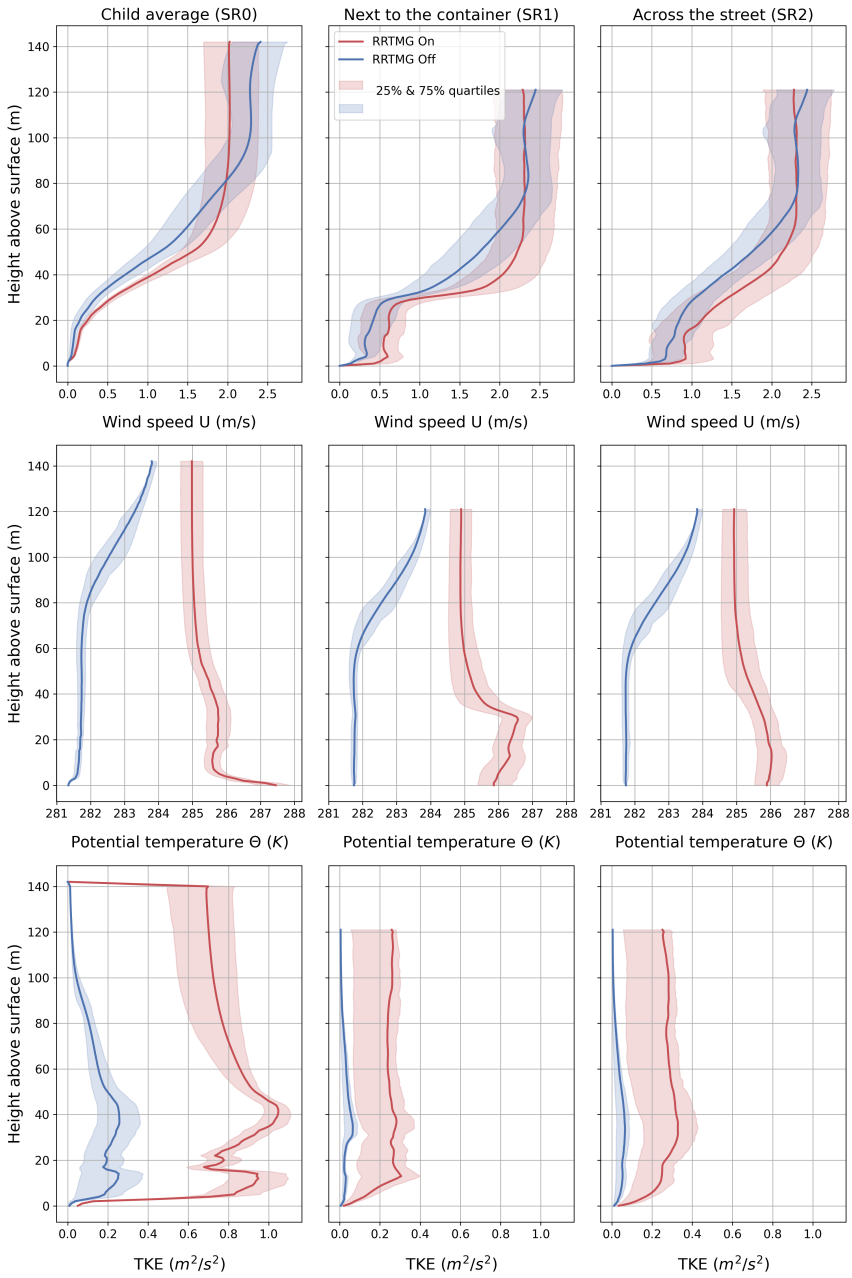

Figure 4.7: Mean profiles for wind, potential temperature and TKE over statistical regions 0-2 between 07:15-09:15. The shaded regions show the 25th and 75th percentiles.

over the whole child domain. The situation described by these simulations starts off as stable in RRTMG Off (Kurppa et al., 2020b), which is typical for a nocturnal BL (Stull, 1988; Oke, 1987). After the sun starts to rise at the beginning of the run in RRTMG On, the surface experiences more rapid warming than the atmosphere above it, which leads to an unstable stratification in the air pillar. The potential temperature profiles increased in RRTMG On by 1.1% for the whole child domain, which is to be expected due to the

additional energy input of solar radiation (Oke, 1987). The change in the shape of the profiles within the canyon looks similar to previous studies conducted by Qu et al. (2012). RRTMG On shows unstable regions with a decrease in potential temperature with an increase in altitude. SR1 and SR2 are both confined in the Mäkelänkatu street caynon, which means that the amounts of direct sunlight is smaller compared to open fields and wider boulevards. There is a sharp decrease in temperature due to the surface being at a warmer temperature in the child domain, but this is not visible in the street canyon, as the sun is yet to heat the surface directly. In the canyon profiles the contrast between the UCL and the overlying flow is visible as a decrease in potential temperature and is again stronger on the windward side.

4.3.2 Turbulent kinetic energy (TKE)

TKE seems to behave similarly as the mean wind with increasing until the top of the UCL, after which it stays nearly constant with height (figure 4.7). The new unstable situation leads to thermals, which increase the amount of turbulence and therefore the thermal production term of TKE (2.8) (Oke, 1987). The larger wind speeds associated with the unstable run also lead to an increase in the mechanical production term, due to there being a stronger vertical gradient in wind speed. Over the whole child domain, the average column TKE increased by a magnitude of 5.4. The magnitude of TKE in the canyon shows around 60% smaller values compared to the full domain average, while the difference between the runs is closer to one magnitude within the canyon. The location of the largest TKE values in the canyon is found at a height of 20 meters, which is close to the height of the southwestern side of the street and therefore at the top of the UCL. This location is coincides well with the height found by Giometto et al. (2016) in the cross canyon flow case, whereas the TKE spike was closer to two times the height of the UCL in flow along the canyon. After 40 meters above the ground TKE shows nearly no change with increased height, which is typical for constant flux layers in previous tower measurements (Christen et al., 2009). In the child average, however, TKE decreases

slightly until it reaches the top of the vertical nesting dimension of the child. All variables also show a larger spread in RRTMG On, with the exception of potential temperature above 60 meters.

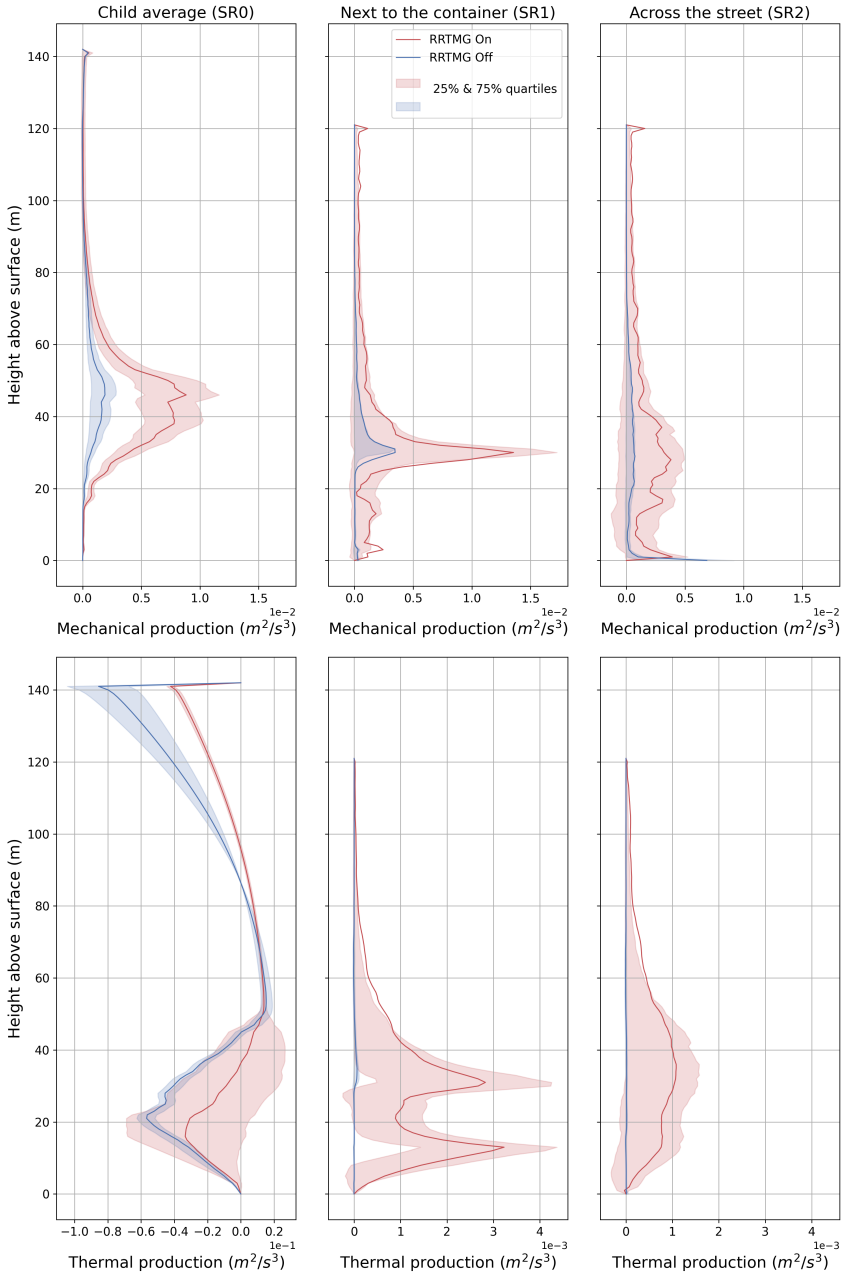

Figure 4.8: Mean profiles of mechanical and thermal TKE production terms over statistical regions 0-2 between 07:15-09:15. The shaded regions show the 25th and 75th percentiles. The child average thermal production term does not share the x-axis with the two smaller statistical regions.

Figure 4.8 shows the profiles of the two production terms in equation 2.8. Both terms are larger in magnitude and variation for RRTMG On, with the small exception of thermal

production having a larger spread above 100 meters in RRTMG Off and averaged over the whole child domain (SR0). Both canyon profiles (SR1 & SR2) show the constant flux layer above the peak of both production terms (Stull, 1988; Christen et al., 2009). The thermal production terms for both runs in the profiles within the canyon are negligible as the they are at least an order of magnitude smaller compared to the mechanical production term. Similar results were found in Lundquist and Chan (2007), where the thermal production was found to be negligible even for a daytime case. The mechanical production is more spread out for the domain average and for the opposite side of the street compared to the profile next to the container as the air has mixed during the crossing of the canyon. The strong vertical gradient in wind speed in Figure 4.7 correlates with the large spike in mechanical production at twice the height of the UCL, which was also the case in Giometto et al. (2016).

5. Conclusions

The aim of this thesis was to understand and quantify how radiative transfer and thermal turbulence alter the flow and turbulence in a real city environment in Helsinki. The LES model PALM was used to conduct two different runs, with the difference being the inclusion of the radiative processes in RRTMG On. The model setup consisted of three nesting domains within each other and with an increase in spatial resolution up to one meter per grid cell in the child domain, which is an extremely high resolution compared to typical weather models. The radiative transfer and longwave and shortwave radiations were calculated by the external library, RRTMG, and then fed into the surface models embedded in PALM for solving the energy balance. Meterological boundary conditions were supplied by FMI's numerical weather prediction model, MEPS/HARMONIE. Surface data information required by the interactions between the atmosphere and the surface were applied from geospatial surface data maps.

The main method used was spatial and temporal averages of meteorological variables such as the wind components, air and surface temperatures. Turbulent fluxes were also used to calculate the production terms in the turbulent kinetic energy budget equation to quantify the amount of turbulence present.

The results show that the initially neutrally stratified situation in RRTMG Off became unstable with RRTMG On. It was found that the differential heating caused by the solar heating combined with the layout of the surface elements lead to the street canyons experiencing heating mostly on the facets directed towards northeast, with cooling on surfaces facing southwest. This leads to an imbalance in the vertical distribution of air temperatures and alternating rising and sinking motions, depending on whether or not

the facet experienced heating or cooling. The wind direction change halfway through the run started to break down a canyon vortex, which formed in Mäkelänkatu, but with the additional forcing of solar radiation the horizontal motions replacing regions of ascent acted as a restoring forcing for the vortex. This effect is not fully responsible for the structure of the vortex, due to the change in wind direction being smaller for RRTMG On. RRTMG On shows larger thermal turbulent production due to the larger variability in the temperature and vertical wind field. The profiles of the production terms show an increase of both terms with RRTMG On due to the thermals created by the heteregenous warming. Increased horizontal wind speeds and their variability in RRTMG On is also visible from the production of mechanical turbulence, as the turbulent flux of momentum increases due to larger wind speeds. Thermal production was mainly negligible within the street canyon, as the term at least an order of magnitude smaller than mechanical production for both runs.

Further research is required to get a definitive answer to see if the computational cost of solving for the radiative transfer is worth including in these kinds of simulations in general. It would seem that at least in low wind conditions, such as the one in this case, the role of radiative transfer processes is large enough to support including these processes in simulations. Furthermore, the effect of thermal turbulence on ventilation and air quality were not focused on in this thesis and have to be assessed separately. The next steps could be to create more runs for different meteorological conditions by for example altering the wind direction and speed or using another time of day or year. Moreover, the results can differ for other cities at different latitudes and climates. The building materials were originally chosen to represent German cities, hence why their physical properties could be different from the materials used in Helsinki.

All in all, radiative processes seems to have a larger effect on flow at low levels and locally in the Mäkelänkatu street canyon compared to the whole child domain, but the TKE production terms showed only a negligible difference when comparing thermal and mechanical production.

Acknowledgements

The radiation simulation conducted in this study is based an earlier case by Kurppa et al. (2020b). The results obtained in that study mainly focused on aerosols, but the data from that study were important in planning and analyzing the consequent runs. The article therefore provided a baseline for this thesis and I am grateful for the lessons I learned in creating and running these kinds of simulations.

I would also like to thank my supervisors, Leena Järvi and Mona Kurppa. I could not ask for better supervisors to provide all the tools and information needed to be able to do get to this point.

The background data for the meteorological forcing were obtained from FMI's MEPS/HARMONIE model and made sure that both RRTMG On and Off had the same initial conditions. The multitude of input data required by the modules in PALM and used by RRTMG were obtained from open data provided by the city of Helsinki, Helsinki Region Service Authority (HSY) and the Geological Land Survey of Finland (GTK).

I would like to thank my family for always supporting me and reminding me to not only focus on work and studies. Thank you also to my friends, especially Janina and Aurora for your peer support during all the courses and projects. Finally I want to thank you Laura for your endless support during this journey.

Bibliography

Argyropoulos, C. and Markatos, N. (2015). Recent advances on the numerical modelling of turbulent flows. *Applied Mathematical Modelling*, 39(2):693–732.

Belda, M., Resler, J., Geletič, J., Krč, P., Maronga, B., Sühring, M., Kurppa, M., Kanani-Sühring, F., Fuka, V., Eben, K., Benešová, N., and Auvinen, M. (2020). Sensitivity analysis of the PALM model system 6.0 in the urban environment. *Geoscientific Model Development Discussions*, pages 1–32.

Bottillo, S., De Lieto Vollaro, A., Galli, G., and Vallati, A. (2014). CFD modeling of the impact of solar radiation in a tridimensional urban canyon at different wind conditions. *Solar Energy*, 102:212–222.

Christen, A., Rotach, M. W., and Vogt, R. (2009). The Budget of Turbulent Kinetic Energy in the Urban Roughness Sublayer. *Boundary-Layer Meteorology*, 131(2):193–222.

Dimitrova, R., Sini, J.-F., Richards, K., Schatzmann, M., Weeks, M., Perez García, E., and Borrego, C. (2009). Influence of thermal effects on the wind field within the urban environment. *Boundary-Layer Meteorology*, 131:223–243.

Dylla, H. (2019). Pavement thermal performance and contribution to urban and global climate. `https://www.fhwa.dot.gov/pavement/sustainability/articles/pavement_thermal.cfm`.

FMI (2017). Finnish meteorological institute open data. `https://www.ilmatieteenlaitos.fi/havaintojen-lataus`, date accessed 2021/03/05.

Gehrke, K. F., Sühring, M., and Maronga, B. (2020). Modeling of land-surface interactions in the PALM model system 6.0: Land surface model description, first evaluation, and sensitivity to model parameters. *Geoscientific Model Development Discussions*, pages 1–34.

Gillner, S., Vogt, J., Tharang, A., Dettmann, S., and Roloff, A. (2015). Role of street trees in mitigating effects of heat and drought at highly sealed urban sites. *Landscape and Urban Planning*, 143:33–42.

Giometto, M., Christen, A., Meneveau, C., Fang, J., Krafczyk, M., and Parlange, M. (2016). Spatial characteristics of roughness sublayer mean flow and turbulence over a realistic urban surface. *Boundary-layer meteorology*, 160(3):425–452.

Gross, G. (2012). Effects of different vegetation on temperature in an urban building environment. micro-scale numerical experiments. *Meteorologische Zeitschrift*, 21(4):399–412.

GTK (2018). Maaperä: Karttatasot WFS-rajapinnassa - Geological Survey of Finland.

Guerreiro, S. B., Dawson, R. J., Kilsby, C., Lewis, E., and Ford, A. (2018). Future heatwaves, droughts and floods in 571 European cities. *ENVIRONMENTAL RESEARCH LETTERS*, 13(3).

Harris, C. R., Millman, K. J., van der Walt, S. J., Gommers, R., Virtanen, P., Cournapeau, D., Wieser, E., Taylor, J., Berg, S., Smith, N. J., Kern, R., Picus, M., Hoyer, S., van Kerkwijk, M. H., Brett, M., Haldane, A., del Río, J. F., Wiebe, M., Peterson, P., Gérard-Marchant, P., Sheppard, K., Reddy, T., Weckesser, W., Abbasi, H., Gohlke, C., and Oliphant, T. E. (2020). Array programming with NumPy. *Nature*, 585(7825):357–362.

Hellsten, A., Ketelsen, K., Sühring, M., Auvinen, M., Maronga, B., Knigge, C., Barmpas, F., Tsegas, G., Moussiopoulos, N., and Raasch, S. (2021). A nested multi-scale system

implemented in the large-eddy simulation model PALM model system 6.0. *Geoscientific Model Development*, 14(6):3185–3214.

Hooff, T. V., Blocken, B., and Tominaga, Y. (2017). On the accuracy of CFD simulations of cross-ventilation flows for a generic isolated building: Comparison of RANS, LES and experiments. *Building and Environment*, 114:148–165.

HRI (2018). Helsingin rakennukset - helsinki region infoshare. `https://hri.fi/data/dataset/helsingin-rakennukset`.

HSY (2017). Pääkaupunkiseudun maanpeiteaineisto - helsinki region environmental services authority. `https://www.hsy.fi/ymparistotieto/avoindata/avoin-data---sivut/paakaupunkiseudun-maanpeiteaineisto/`.

Iacono, M. J., Mlawer, E. J., Clough, S. A., and Morcrette, J.-J. (2000). Impact of an improved longwave radiation model, RRTM, on the energy budget and thermodynamic properties of the NCAR community climate model, CCM3. *Journal of Geophysical Research: Atmospheres*, 105(D11):14873–14890.

Karttunen, S. (2020). The effect of street vegetation configuration on the pedestrian-level aerosol mass concentrations in a wide street canyon. *University of Helsinki*.

Krč, P., Resler, J., Sühring, M., Schubert, S., Salim, M. H., and Fuka, V. (2021). Radiative transfer model 3.0 integrated into the PALM model system 6.0. *Geoscientific Model Development*, 14(5):3095–3120.

Kurppa, M. (2020a). Novel large-eddy simulation modelling for urban air quality. *University of Helsinki*.

Kurppa, M. (2020b). Python scripts for evaluating PALM simulations against mobile air quality observations on Mäkelänkatu in Helsinki, Finland. zenodo. Accessed on 5/2021.

Kurppa, M., Balling, A., Karttunen, S., Kuuluvainen, H., Järvi, L., Niemi, J. V., Pirjola, L., Rönkkö, T., and Timonen, H. (2020a). Mobile and stationary air pollution mea-

surements around an air quality monitoring site on Mäkelänkatu in Helsinki, Finland. https://doi.org/10.5281/zenodo.3828508.

Kurppa, M., Roldin, P., Strömberg, J., Balling, A., Karttunen, S., Kuuluvainen, H., Niemi, J. V., Pirjola, L., Rönkkö, T., Timonen, H., Hellsten, A., and Järvi, L. (2020b). Sensitivity of spatial aerosol particle distributions to the boundary conditions in the PALM model system 6.0. *Geoscientific Model Development*, 13(11):5663–5685.

Lundquist, J. K. and Chan, S. T. (2007). Consequences of Urban Stability Conditions for Computational Fluid Dynamics Simulations of Urban Dispersion. *Journal of Applied Meteorology and Climatology*, 46(7):1080–1097.

Maronga, B., Banzhaf, S., Burmeister, C., Esch, T., Forkel, R., Fröhlich, D., Fuka, V., Gehrke, K. F., Geletič, J., Giersch, S., Gronemeier, T., Groß, G., Heldens, W., Hellsten, A., Hoffmann, F., Inagaki, A., Kadasch, E., Kanani-Sühring, F., Ketelsen, K., Khan, B. A., Knigge, C., Knoop, H., Krč, P., Kurppa, M., Maamari, H., Matzarakis, A., Mauder, M., Pallasch, M., Pavlik, D., Pfafferott, J., Resler, J., Rissmann, S., Russo, E., Salim, M., Schrempf, M., Schwenkel, J., Seckmeyer, G., Schubert, S., Sühring, M., von Tils, R., Vollmer, L., Ward, S., Witha, B., Wurps, H., Zeidler, J., and Raasch, S. (2020). Overview of the PALM model system 6.0. *Geoscientific Model Development*, 13(3):1335–1372.

Meehl, G. and Tebaldi, C. (2004). More intense, more frequent, and longer lasting heat waves in the 21st century. *SCIENCE*, 305(5686):994–997.

Mirzanamadi, R., Johansson, P., and Grammatikos, S. (2018). Thermal properties of asphalt concrete: A numerical and experimental study. *Construction and Building Materials*, 158:774–785.

Nazarian, N., Krayenhoff, E., and Martilli, A. (2020). A one-dimensional model of turbulent flow through "urban" canopies (MLUCM v2.0): updates based on large-eddy simulation. *Geoscientific Model Development*, 13:937–953.

Oke, T. (1988). The urban energy balance. *Progress in Physical Geography: Earth and Environment*, 12(4):471–508.

Oke, T. R. (1987). *Boundary Layer Climates*. Springer.

PALM (2021). PALM technical documentation: Radiation. `https://palm.muk.uni-hannover.de/trac/wiki/doc/tec/radiation`, date accessed 15/4/2021.

Park, C., Ha, J., and Lee, S. (2017). Association between three-dimensional built environment and urban air temperature: Seasonal and temporal differences. *Sustainability*, 9:1338.

Park, S.-B. and Baik, J.-J. (2013). A large-eddy simulation study of thermal effects on turbulence coherent structures in and above a building array. *Journal of Applied Meteorology and Climatology*, 52(6):1348–1365.

Pfafferott, J., Rißmann, S., Sühring, M., Kanani-Sühring, F., and Maronga, B. (2020). Building indoor model in PALM model system 6.0: Indoor climate, energy demand, and the interaction between buildings and the urban climate. *Geoscientific Model Development Discussions*, pages 1–11.

Piringer, M., Grimmond, C., Joffre, S., Mestayer, P., Middleton, D., Rotach, M., Baklanov, A., De Ridder, K., Ferreira, J., Guilloteau, E., Karppinen, A., Martilli, A., Masson, V., and Tombrou, M. (2002). Investigating the surface energy budget in urban areas - recent advances and future needs. *Water, Air, & Soil Pollution: Focus*, 2:1–16.

Qu, Y., Milliez, M., Musson-Genon, L., and Carissimo, B. (2012). Numerical study of the thermal effects of buildings on low-speed airflow taking into account 3D atmospheric radiation in urban canopy. *Journal of Wind Engineering and Industrial Aerodynamics*, 104-106:474–483. 13th International Conference on Wind Engineering.

Resler, J., Krč, P., Belda, M., Juruš, P., Benešová, N., Lopata, J., Vlček, O., Damašková, D., Eben, K., Derbek, P., Maronga, B., and Kanani-Sühring, F. (2017). PALM-USM

v1.0: A new urban surface model integrated into the PALM large-eddy simulation model. *Geoscientific Model Development*, 10(10):3635–3659.

Salim, M. H., Schubert, S., Resler, J., Krč, P., Maronga, B., Kanani-Sühring, F., Sühring, M., and Schneider, C. (2020). Importance of radiative transfer processes in urban climate models: A study based on the PALM model system 6.0. *Geoscientific Model Development Discussions*, pages 1–55.

Santamouris, M. and Yun, G. Y. (2020). Recent development and research priorities on cool and super cool materials to mitigate urban heat island. *Renewable Energy*, 161:792–807.

Stewart, I. D. and Oke, T. R. (2012). Local climate zones for urban temperature studies. *Bulletin of the American Meteorological Society*, 93(12):1879–1900.

Strömberg, J. and Auvinen, M. (2020). Raster4H: Raster datasets for helsinki area. `http://doi.org/10.5281/zenodo.3839462`.

Stull, R. B. (1988). *An Introduction to Boundary Layer Meteorology*. Springer.

Száraz, L. (2014). The impact of urban green spaces on climate and air quality in cities. *Geographical Locality Studies*, 2:326–354.

Tan, Z., Lau, K. K.-L., and Ng, E. (2016). Urban tree design approaches for mitigating daytime urban heat island effects in a high-density urban environment. *Energy and Buildings*, 114:265–274. SI: Countermeasures to Urban Heat Island.

Tominaga, Y. and Stathopoulos, T. (2010). Numerical simulation of dispersion around an isolated cubic building: Model evaluation of RANS and LES. *Building and Environment*, 45:2231–2239.

United Nations (2019). World urbanization prospects: The 2018 revision (ST/ESA/SER.A/420). *New York: United Nations*.